A stable partitioned FSI algorithm for rigid bodies and incompressible flow in three dimensions

J. W. Banks[a,1,2], W. D. Henshaw[a,1,3], D. W. Schwendeman[a,1,3], Qi Tang[a,4,*]

[a] *Department of Mathematical Sciences, Rensselaer Polytechnic Institute, Troy, NY 12180, USA.*

Abstract

This paper describes a partitioned algorithm for fluid-structure interaction (FSI) that couples the motion of rigid bodies and incompressible flow, and that remains stable for bodies of any mass. It extends the *added-mass partitioned* (AMP) algorithm developed in [1, 2] to three-dimensional geometries and parallel computations. Moving composite grids are used to represent the moving geometry and a domain-decomposition approach is used to implement the AMP algorithm on parallel distributed-memory computers. The algorithm is verified and validated though several benchmark problems, including the motion of a sphere in a viscous incompressible fluid and the interaction of a bi-leaflet mechanical heart valve and a pulsating fluid. Numerical simulations confirm that the AMP algorithm remains stable, without sub-iterations, for light and even zero-mass three-dimensional rigid bodies of general shapes. These benchmark problems are further used to examine the parallel performance of the algorithm and to investigate the conditioning of the new linear system resulting from the AMP interface condition. The linear system for the AMP algorithm is shown to have a similar conditioning to that for a pressure equation in a traditional partitioned scheme.

Keywords: fluid-structure interaction; moving overlapping grids; incompressible Navier-Stokes; partitioned schemes; added-mass; added-damping; rigid bodies

[*] Department of Mathematical Sciences, Rensselaer Polytechnic Institute, 110 8th Street, Troy, NY 12180, USA.
Email addresses: banksj3@rpi.edu (J. W. Banks), henshw@rpi.edu (W. D. Henshaw), schwed@rpi.edu (D. W. Schwendeman), tangq3@rpi.edu (Qi Tang)

[1] This work was supported by contracts from the U.S. Department of Energy ASCR Applied Math Program.
[2] Research supported by a U.S. Presidential Early Career Award for Scientists and Engineers.
[3] Research supported by the National Science Foundation under grant DMS-1519934.
[4] Research supported by the Eliza Ricketts Postdoctoral Fellowship.

Contents

1. Introduction

In this work, we consider three-dimensional fluid-structure interaction (FSI) problems involving the motion of rigid bodies in a viscous incompressible fluid. A novel partitioned FSI algorithm, referred to as the AMP-RB scheme, was described previously in our two-part series [1, 2] for FSI problems in two space dimensions. In these papers, it was proved analytically and verified numerically that the algorithm is stable without sub-iterations for bodies of any mass including bodies of zero mass. The general formulation in three dimensions was indicated in [2], but the algorithm was only implemented and verified in two dimensions. The current work extends the algorithm for three-dimensional FSI problems using the moving overlapping grid framework [3], and verifies its stability and accuracy through several challenging benchmark problems.

The FSI regime considered here has drawn significant attention in recent years due to its great practical importance. Besides the moving overlapping grid approach, a variety of classical numerical techniques for moving complex geometries have been extended to this regime, including arbitrary Lagrangian–Eulerian (ALE) methods [4–6], level-set methods [7, 8], fictitious domain methods [9], embedded boundary methods [10] and immersed boundary methods [11–23]. Recently, new approaches to handle moving geometries have also been developed for this regime, such as methods based on boundary integral equations [24] and implicit mesh discontinuous Galerkin methods [25, 26].

Many of the FSI algorithms for simulating rigid bodies and incompressible flow, including our AMP-RB scheme, can be categorized as *partitioned*, in which different solvers are used to solve the fluid and structure equation separately with the two solvers coupled through interface conditions. In traditional partitioned (TP-RB) schemes, the typical coupling is implemented sequentially by first using the motion of the bodies as boundary conditions for the fluid solver, and then evaluating forces and torques on the bodies from the computed fluid stress and advancing the bodies. These schemes have been very popular due to their relative simplicity in adapting existing fluid and solid solvers, but they are known to suffer from numerical instabilities especially when bodies become relatively light. As found in many previous results as well as our own investigation [1], the primary numerical instability is due to well known added-mass effects. In [1], a secondary numerical instability, referred to as the added-damping instability, was first investigated carefully and found to be equally important for certain partitioned schemes when simulating problems involving low Reynolds numbers or when the primary motion of the body is rotational and not translational when added-mass effects dominate. The interested reader is referred to [1] for further discussion on added-mass and added-damping effects. To overcome these instabilities, TP-RB schemes often rely on under-relaxed sub-iterations, see [6, 15, 21, 27, 28] for example. In the AMP-RB schemes, however, a novel coupling strategy, the AMP interface condition, is used to avoid potentially expensive sub-iterations. This interface condition, first described in [1, 2], is reviewed briefly here because it serves as an essential element of the current work.

Aside from the typical coupling scheme used in many TP-RB schemes and the AMP interface condition in this work, other coupling strategies have been proposed in the literature with the aim of suppressing added-mass instabilities, see [17, 20, 23] for example. Through this work, the stability bound for the ratio of the density of the body to that of the fluid has improved over the years. For instance, the immersed boundary method [23] remains stable for a density ratio as low as 10^{-4}. In this approach, a set of equations that couples the pressure with the motion for the body is exposed through an approximate block LU factorization. The treatment bears some similarity with the handling of added-mass effect in the AMP-RB scheme except that the AMP interface condition used here is derived at a continuous level, which would facilitate the development of high-order accurate schemes. More details of these coupling strategies can be found in the introduction of our previous work [1]. Recently, Kempe, Fröhlich and their collaborators proposed two other coupling strategies for immersed boundary methods applied to spherical particles in [29, 30]. Their numerical results demonstrate that both of the approaches are stable for spherical particles of any mass including zero mass without sub-iterations. In [29], a virtual mass with an ad hoc parameter is incorporated into the equations of motion of the rigid body. This approach appears to have a similar formulation as the added-damping tensor in the AMP interface condition. However, the added-damping tensor in our approach is derived from a continuous level for bodies of general shapes; therefore, it is not limited to spherical bodies and no ad hoc parameters are needed. We note that there was an added-damping parameter introduced in [1] for the purpose of analysis, but it was set to one for all of the subsequent simulations as suggested by the stability analysis. Another difference between the approach in [29] and one discussed here is that the added-damping tensor is only used to handle added-damping effects while the virtual mass in [29] is used to handle both

added-mass and added-damping effects. In their more recent work [30], the mass and inertia in a Lagrangian layer surrounding the particle surface are exposed at a continuous level and incorporated into the equations of motions of the rigid body. This results in a strongly coupled FSI scheme that only needs a semi-implicit update and avoids sub-iterations completely. Although [30] only considered spherical particles, this new approach is more promising and seems extendible to bodies of general shape.

In previous work [1, 2], the stability of the AMP-RB algorithm was analyzed for selected model problems and verified for a range of two-dimensional benchmark problems. In the current work, numerical simulations in three dimensions are used to show that the AMP-RB scheme is stable without sub-iterations for bodies of general shape, including spherical particles and two flapping *leaflets*, each in the shape of a thin half-disk. The benchmark problem involving leaflets is generalized from a bi-leaflet mechanical heart valve. The bi-leaflet mechanical heart valve simulation is an important application of the current FSI regime and has been simulated previously by many FSI algorithms such as those discussed in [15, 31–36]. The review paper [37] summarizes the practical and numerical challenges in this problem. Our particular attention is on the strong added-mass effects in this simulation due to a very small moment of inertia of the leaflets. Numerical instabilities have been reported previously in [15, 35, 36], in which sub-iterations, typically with Aitken's accelerations, are used to stabilize the FSI algorithms. Apart from difficulties associated with added-mass effects, this problem is challenging since the two leaflets are hinged and thus follow a constrained motion. To successfully simulate this FSI problem, many building blocks need to be handled carefully, such as the implementation of the AMP-RB algorithm in three dimensions, generating and moving the grids within the overlapping grid framework, forming accurate surface quadratures on overlapping surface grids, and implementing the full algorithm in parallel. These factors have motivated us to verify the stability and applicability of the AMP-RB scheme in the overlapping grid framework through this challenging FSI application.

The AMP-RB scheme has been implemented in serial and parallel within the *Overture* object-oriented framework. This implementation, as well as the numerical examples presented in this work, is freely available at `overtureFramework.org`. The parallel implementation follows a domain-decomposition approach on overlapping grids discussed in [38]. Note that the AMP-RB scheme discussed herein follows the line of research on AMP schemes for various FSI regimes, including inviscid compressible fluids coupled to rigid solids [39], linearly elastic solids [40], nonlinear elastic solids [41], as well as incompressible fluids coupled to elastic bulk solids [42], elastic structural shells [43] and deforming beams [44].

The remaining sections of the paper are organized as follows. The governing equations are given in Section 2. The details of the AMP-RB algorithm are outlined in 3, including a brief review of the AMP interface condition and the time-stepping algorithm. Section 4 presents the numerical approach for three dimensions. This section includes a brief outline of the moving overlapping grid approach, a description of the approach for computing surface integrals on bodies covered by multiple overlapping grids, and a discussion of the parallel implementation. Numerical results are presented in Section 5 and concluding remarks as well as future directions are given in Section 6. A collision model designed specifically for the heart-valve problem is discussed in Appendix A.

2. Governing equations

We consider an FSI problem involving one or more rigid bodies fully immersed in an incompressible fluid as illustrated in Figure 1. The fluid occupies the domain, $\mathbf{x} \in \Omega(t)$ at a time t, and is governed by the incompressible Navier-Stokes equations,

$$\frac{\partial \mathbf{v}}{\partial t} + (\mathbf{v}\cdot\nabla)\mathbf{v} = \frac{1}{\rho}\nabla\cdot\boldsymbol{\sigma}, \qquad \mathbf{x}\in\Omega(t), \tag{1}$$

$$\nabla\cdot\mathbf{v} = 0, \qquad \mathbf{x}\in\Omega(t), \tag{2}$$

where $\mathbf{v} = \mathbf{v}(\mathbf{x},t)$ is the fluid velocity, $\boldsymbol{\sigma} = \boldsymbol{\sigma}(\mathbf{x},t)$ is the stress tensor, and ρ is the (constant) fluid density. The fluid stress tensor is given by

$$\boldsymbol{\sigma} = -p\mathbf{I} + \boldsymbol{\tau}, \qquad \boldsymbol{\tau} = \mu\left[\nabla\mathbf{v} + (\nabla\mathbf{v})^T\right], \tag{3}$$

where $p = p(\mathbf{x}, t)$ is the pressure, $\mathbf{I}$ is the identity tensor, $\boldsymbol{\tau}$ is the viscous stress tensor and μ is the (constant) dynamic viscosity. Equations (1)–(3) can be used to derive an elliptic equation for the pressure satisfying

$$\Delta p = -\rho \nabla \mathbf{v} : (\nabla \mathbf{v})^T, \qquad \mathbf{x} \in \Omega(t), \tag{4}$$

where

$$\nabla \mathbf{v} : (\nabla \mathbf{v})^T \stackrel{\text{def}}{=} \sum_{i=1}^{3} \sum_{j=1}^{3} \frac{\partial v_i}{\partial x_j} \frac{\partial v_j}{\partial x_i},$$

with an additional boundary condition, $\nabla \cdot \mathbf{v} = 0$ for $\mathbf{x} \in \partial\Omega(t)$, see [45] for more details. In practice, our time-stepping scheme uses the velocity-pressure form of the incompressible Navier-Stokes equations, in which the continuity equation (2) is replaced by the Poisson equation (4).

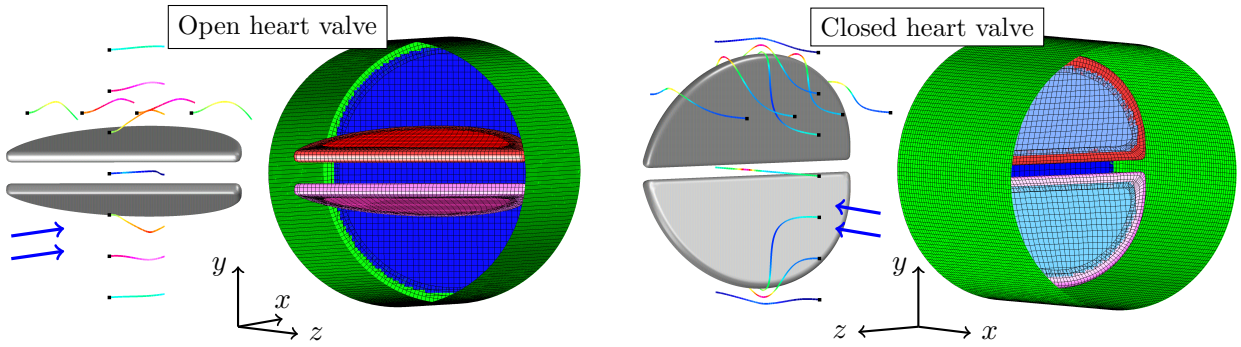

Figure 1: Flow past the bi-leaflet mechanical heart valve at the open and closed states. Note the change of the flow directions at the two positions. Computed streamlines (colored by the flow speed) and the composite grids are presented.

Within the FSI problem, each body has mass m_b and moment of inertia $\mathbf{I}_b$ and occupies the domain $\Omega_b(t)$. The dynamics of the body are characterized by

$\mathbf{a}_b(t) \in \mathbb{R}^3$: linear acceleration of the centre of mass,
$\mathbf{b}_b(t) \in \mathbb{R}^3$: angular acceleration of the centre of mass,
$\mathbf{v}_b(t) \in \mathbb{R}^3$: velocity of the centre of mass,
$\boldsymbol{\omega}_b(t) \in \mathbb{R}^3$: angular velocity,
$\mathbf{x}_b(t) \in \mathbb{R}^3$: position of the centre of mass,
$E_b(t) \in \mathbb{R}^{3\times 3}$: matrix with columns being the principle axes of inertia.

The motion of each rigid body is determined by a surface integral of the fluid traction $\boldsymbol{\sigma}\mathbf{n}$ along the interface $\Gamma_b(t) = \bar{\Omega}(t) \cap \bar{\Omega}_b(t)$, where $\boldsymbol{\sigma}$ is the fluid stress and $\mathbf{n}$ is the unit outward normal at the interface. In three dimensions, the rigid body has six degrees of freedom and its motion satisfies the Newton-Euler equations,

$$m_b \mathbf{a}_b = \int_{\Gamma_b} \boldsymbol{\sigma}\mathbf{n}\, dS + \mathbf{f}_e, \tag{5}$$

$$\mathbf{I}_b \mathbf{b}_b = -\boldsymbol{\omega}_b \times \mathbf{I}_b \boldsymbol{\omega}_b + \int_{\Gamma_b} (\mathbf{r} - \mathbf{x}_b) \times \boldsymbol{\sigma}\mathbf{n}\, dS + \mathbf{g}_e, \tag{6}$$

$$\dot{\mathbf{v}}_b = \mathbf{a}_b, \tag{7}$$

$$\dot{\boldsymbol{\omega}}_b = \mathbf{b}_b, \tag{8}$$

$$\dot{\mathbf{x}}_b = \mathbf{v}_b, \tag{9}$$

$$\dot{E}_b = \boldsymbol{\omega}_b \times E_b, \tag{10}$$

where $\mathbf{r}$ denotes a point on the surface of the body, and $\mathbf{f}_e$ and $\mathbf{g}_e$ are an applied external force and torque on the body, respectively.

The velocity of the fluid is coupled to that of each rigid body on its surface Γ_b by the matching condition

$$\mathbf{v}(\mathbf{r}(t),t) = \dot{\mathbf{r}}(t), \qquad \mathbf{r}(t) \in \Gamma_b. \tag{11}$$

The motion of a point $\mathbf{r}(t)$ on the surface of the body is given by a translation together with a rotation about the initial centre of mass,

$$\mathbf{r}(t) = \mathbf{x}_b(t) + R(t)(\mathbf{r}(0) - \mathbf{x}_b(0)), \tag{12}$$

where $R(t)$ is the rotation matrix given by

$$R(t) = E_b(t)E_b^T(0). \tag{13}$$

The velocity $\dot{\mathbf{r}}(t)$ in (11) is determined by differentiating (12), and using (9), (10) and (13) to find

$$\dot{\mathbf{r}}(t) = \mathbf{v}_b(t) + \boldsymbol{\omega}_b(t) \times (\mathbf{r}(t) - \mathbf{x}_b(t)), \qquad \mathbf{r}(t) \in \Gamma_b. \tag{14}$$

We also use the acceleration of a point on the surface of the body for the AMP-RB algorithm, and this is given by

$$\ddot{\mathbf{r}}(t) = \mathbf{a}_b(t) + \mathbf{b}_b(t) \times (\mathbf{r}(t) - \mathbf{x}_b(t)) + \boldsymbol{\omega}_b(t) \times \big[\boldsymbol{\omega}_b(t) \times (\mathbf{r}(t) - \mathbf{x}_b(t))\big], \qquad \mathbf{r}(t) \in \Gamma_b. \tag{15}$$

3. The AMP-RB algorithm

In this section, we describe the interface conditions used in the AMP-RB scheme to handle added-mass and added-damping effects arising from the forces and torques on the rigid body due to fluid. Since the interface conditions and the AMP-RB scheme were derived in our previous paper [2], we give only a brief summary here for completeness.

3.1. The added-mass and added-damping interface conditions

To handle added-mass effects, the fluid and body accelerations on the interface are matched. Taking a time derivative of the matching conditions in (11) and using the acceleration of a point on the body given in (15), we obtain

$$\partial_t \mathbf{v} + (\dot{\mathbf{r}} \cdot \nabla)\mathbf{v} = \mathbf{a}_b + \mathbf{b}_b \times (\mathbf{r} - \mathbf{x}_b) + \boldsymbol{\omega}_b \times \big[\boldsymbol{\omega}_b \times (\mathbf{r} - \mathbf{x}_b)\big], \qquad \mathbf{r} \in \Gamma_b,$$

and using the momentum equation (1) gives

$$-\frac{1}{\rho}\Big[\nabla p - \mu\Delta\mathbf{v}\Big] = \mathbf{a}_b + \mathbf{b}_b \times (\mathbf{r} - \mathbf{x}_b) + \boldsymbol{\omega}_b \times \big[\boldsymbol{\omega}_b \times (\mathbf{r} - \mathbf{x}_b)\big], \qquad \mathbf{r} \in \Gamma_b. \tag{16}$$

The normal component of (16) satisfies

$$\partial_n p = -\rho\mathbf{n}^T\Big(\mathbf{a}_b + \mathbf{b}_b \times (\mathbf{r} - \mathbf{x}_b) + \boldsymbol{\omega}_b \times \big[\boldsymbol{\omega}_b \times (\mathbf{r} - \mathbf{x}_b)\big]\Big) + \mu\mathbf{n}^T\Delta\mathbf{v}, \qquad \mathbf{r} \in \Gamma_b, \tag{17}$$

where $\mathbf{n} = \mathbf{n}(\mathbf{r},t)$ is the outward normal to the body. When the pressure and body accelerations are coupled strongly in the AMP-RB scheme, the condition in (17) is equivalent to a generalized Robin boundary condition for the pressure.

Added-damping effects are treated in the AMP-RB scheme by considering the contributions to the force and torque on the body in (5) and (6), respectively, due to the integrals,

$$\mathcal{F}_\mu(\mathbf{v},\mathbf{v}_b,\boldsymbol{\omega}_b) = \int_{\Gamma_b} \boldsymbol{\tau}\mathbf{n}\, dS, \qquad \mathcal{G}_\mu(\mathbf{v},\mathbf{v}_b,\boldsymbol{\omega}_b) = \int_{\Gamma_b} (\mathbf{r} - \mathbf{x}_b) \times (\boldsymbol{\tau}\mathbf{n})\, dS,$$

involving the viscous shear stress $\boldsymbol{\tau}\mathbf{n}$ of the fluid. The integrals depend on the fluid velocity $\mathbf{v}$, and on the velocity $\mathbf{v}_b$ and angular velocity $\boldsymbol{\omega}_b$ of the body due to its motion. The linearized forms

$$\mathcal{F}_\mu(\mathbf{v},\mathbf{v}_b,\boldsymbol{\omega}_b) \approx \mathcal{F}_\mu(\mathbf{v}^p,\mathbf{v}_b^p,\boldsymbol{\omega}_b^p) - \mathcal{D}^{vv}\,(\mathbf{v}_b-\mathbf{v}_b^p) - \mathcal{D}^{v\omega}\,(\boldsymbol{\omega}_b-\boldsymbol{\omega}_b^p), \tag{18}$$

$$\mathcal{G}_\mu(\mathbf{v},\mathbf{v}_b,\boldsymbol{\omega}_b) \approx \mathcal{G}_\mu(\mathbf{v}^p,\mathbf{v}_b^p,\boldsymbol{\omega}_b^p) - \mathcal{D}^{\omega v}\,(\mathbf{v}_b-\mathbf{v}_b^p) - \mathcal{D}^{\omega\omega}\,(\boldsymbol{\omega}_b-\boldsymbol{\omega}_b^p), \tag{19}$$

about the predicted states $\mathbf{v}^p$, $\mathbf{v}_b^p$ and $\boldsymbol{\omega}_b^p$ are used to expose the dependence of the integrals on the motion of the body. Here, $\mathcal{D}^{vv}$, $\mathcal{D}^{v\omega}$, $\mathcal{D}^{\omega v}$, and $\mathcal{D}^{\omega\omega}$ are *added-damping tensors* derived in [2] as

$$\mathcal{D}^{vv} \stackrel{\text{def}}{=} -\frac{\partial \mathcal{F}_\mu}{\partial \mathbf{v}_b} = -\mu\int_{\Gamma_b}\left\{(\mathbf{I}-\mathbf{n}\mathbf{n}^T)\frac{\partial}{\partial n}\left(\frac{\partial \mathbf{v}}{\partial \mathbf{v}_b}\right)\right\}dS, \tag{20a}$$

$$\mathcal{D}^{v\omega} \stackrel{\text{def}}{=} -\frac{\partial \mathcal{F}_\mu}{\partial \boldsymbol{\omega}_b} = -\mu\int_{\Gamma_b}\left\{(\mathbf{I}-\mathbf{n}\mathbf{n}^T)\frac{\partial}{\partial n}\left(\frac{\partial \mathbf{v}}{\partial \boldsymbol{\omega}_b}\right)\right\}dS, \tag{20b}$$

$$\mathcal{D}^{\omega v} \stackrel{\text{def}}{=} -\frac{\partial \mathcal{G}_\mu}{\partial \mathbf{v}_b} = -\mu\int_{\Gamma_b}[\mathbf{r}-\mathbf{x}_b]_\times\left\{(\mathbf{I}-\mathbf{n}\mathbf{n}^T)\frac{\partial}{\partial n}\left(\frac{\partial \mathbf{v}}{\partial \mathbf{v}_b}\right)\right\}dS, \tag{20c}$$

$$\mathcal{D}^{\omega\omega} \stackrel{\text{def}}{=} -\frac{\partial \mathcal{G}_\mu}{\partial \boldsymbol{\omega}_b} = 2\mu V_b\,\mathbf{I} - \mu\int_{\Gamma_b}[\mathbf{r}-\mathbf{x}_b]_\times\left\{(\mathbf{I}-\mathbf{n}\mathbf{n}^T)\frac{\partial}{\partial n}\left(\frac{\partial \mathbf{v}}{\partial \boldsymbol{\omega}_b}\right)\right\}dS, \tag{20d}$$

where V_b is the volume of the rigid body and the notation $[\mathbf{r}-\mathbf{x}_b]_\times$ denotes the matrix representation of the usual cross product involving the vector $\mathbf{r}-\mathbf{x}_b$. For convenience, a larger composite tensor, $\mathbf{D}(t)\in\mathbb{R}^{6\times 6}$, is defined as

$$\mathbf{D} \stackrel{\text{def}}{=} \begin{bmatrix}\mathcal{D}^{vv} & \mathcal{D}^{v\omega}\\ \mathcal{D}^{\omega v} & \mathcal{D}^{\omega\omega}\end{bmatrix}, \tag{21}$$

and we note that the component tensors in $\mathbf{D}(t)$ can be computed based on their initial states using the transformation

$$\mathcal{D}^{\alpha\beta}(t) = R(t)\,\mathcal{D}^{\alpha\beta}(0)\,R^T(t), \tag{22}$$

where $R(t)$ is the rotation matrix from (13).

Note that the linearizations (18) and (19) can be expressed in terms of the body accelerations $\mathbf{a}_b$ and $\mathbf{b}_b$ as follows:

$$\mathcal{F}_\mu(\mathbf{v},\mathbf{v}_b,\boldsymbol{\omega}_b) \approx \mathcal{F}_\mu(\mathbf{v}^p,\mathbf{v}_b^p,\boldsymbol{\omega}_b^p) - \Delta t\,\mathcal{D}^{vv}\,(\mathbf{a}_b-\mathbf{a}_b^p) - \Delta t\,\mathcal{D}^{v\omega}\,(\mathbf{b}_b-\mathbf{b}_b^p), \tag{23}$$

$$\mathcal{G}_\mu(\mathbf{v},\mathbf{v}_b,\boldsymbol{\omega}_b) \approx \mathcal{G}_\mu(\mathbf{v}^p,\mathbf{v}_b^p,\boldsymbol{\omega}_b^p) - \Delta t\,\mathcal{D}^{\omega v}\,(\mathbf{a}_b-\mathbf{a}_b^p) - \Delta t\,\mathcal{D}^{\omega\omega}\,(\mathbf{b}_b-\mathbf{b}_b^p). \tag{24}$$

where Δt is the discrete time-step in the AMP-RB time-stepping scheme.

The pressure boundary condition in (17) and the linearizations in (23) and (24) are used in the following primary AMP interface condition:

AMP Interface Condition. *The AMP interface conditions on the surface of a rigid body $\mathbf{r}\in\Gamma_b$ for the pressure equation (4) are*

$$\partial_n p + \rho\mathbf{n}^T\Big(\mathbf{a}_b+\mathbf{b}_b\times(\mathbf{r}-\mathbf{x}_b)\Big) = -\rho\mathbf{n}^T\Big(\boldsymbol{\omega}_b\times\big[\boldsymbol{\omega}_b\times(\mathbf{r}-\mathbf{x}_b)\big]\Big) + \mu\mathbf{n}^T\Delta\mathbf{v}, \tag{25}$$

$$\left\{\begin{bmatrix}m_b\,I_{3\times 3} & 0\\ 0 & \mathbf{I}_b\end{bmatrix} + \Delta t\,\mathbf{D}\right\}\begin{bmatrix}\mathbf{a}_b\\ \mathbf{b}_b\end{bmatrix} + \mathbf{F}(p) = -\begin{bmatrix}0\\ \boldsymbol{\omega}_b\times\mathbf{I}_b\boldsymbol{\omega}_b\end{bmatrix} + \mathbf{G}(\mathbf{v}) + \Delta t\,\mathbf{D}\begin{bmatrix}\mathbf{a}_b\\ \mathbf{b}_b\end{bmatrix}, \tag{26}$$

where

$$\mathbf{F}(p) \stackrel{\text{def}}{=} \begin{bmatrix}\displaystyle\int_{\Gamma_b} p\,\mathbf{n}\,dS\\ \displaystyle\int_{\Gamma_b}(\mathbf{r}-\mathbf{x}_b)\times(p\,\mathbf{n})\,dS\end{bmatrix}, \qquad \mathbf{G}(\mathbf{v}) \stackrel{\text{def}}{=} \begin{bmatrix}\mathcal{F}_\mu+\mathbf{f}_e\\ \mathcal{G}_\mu+\mathbf{g}_e\end{bmatrix} = \begin{bmatrix}\displaystyle\int_{\Gamma_b}\boldsymbol{\tau}\mathbf{n}\,dS+\mathbf{f}_e\\ \displaystyle\int_{\Gamma_b}(\mathbf{r}-\mathbf{x}_b)\times(\boldsymbol{\tau}\mathbf{n})\,dS+\mathbf{g}_e\end{bmatrix}. \tag{27}$$

Here Δt is the time-step used in the AMP-RB time-stepping scheme.

The AMP interface conditions given here differ slightly from the ones derived in [2]. First, the signs on the integrals of the two vector components of $\mathbf{F}(p)$ in (27) were incorrect in our previous paper and have been fixed here. Second, an added-damping parameter appeared in the earlier AMP interface conditions for the purpose of studying the stability of the AMP-RB scheme. As mentioned previously, the results of the stability analysis discussed in [1] suggest that this parameter can be taken to be one. This value has been used in the form of the interface conditions given here and so the added-damping parameter does not appear.

3.2. Time-stepping algorithm

Algorithm 1 provides the details of the AMP-RB time-stepping scheme used for the calculations presented in this paper. The algorithm given here follows the ones discussed in our previous work [1, 2], but extended to three dimensions. It is a predictor-corrector-type fractional-step scheme that advances the solution from the time step t^n to t^{n+1}. The algorithm starts with a preliminary body evolution stage consisting of Steps 1 and 2, in which the rigid-body variables and the moving composite grid at the new time step are predicted from the analogous quantities at previous time steps. The moving grid $\mathcal{G}$ in Step 2 is determined by the predicted values for $\mathbf{x}_b$ and E_b using equations (12) and (13), see Section 4.1 for more details. The preliminary stage is followed by the predictor stage consisting of Steps 3–6. In Step 3, the fluid velocity, $\mathbf{v}_\mathbf{i}^\star$, is computed implicitly using the rigid-body velocities predicted in Step 1 for the boundary condition on the surface of the body. Note that the advection and pressure terms in the momentum equation (1) are written as a single term,

$$\mathbf{f}_\mathbf{i}^n \stackrel{\text{def}}{=} \big((\mathbf{v}_\mathbf{i}^n - \mathbf{w}_\mathbf{i}^n) \cdot \nabla_h\big)\mathbf{v}_\mathbf{i}^n + \nabla_h p_\mathbf{i}^n,$$

in Step 3, where the *grid velocity*, $\mathbf{w}_\mathbf{i}^n$, is included as required to express the equations in a moving coordinate system. The ghost points for the velocity calculation at this step are determined by the divergence of the velocity applied on the boundary together with an extrapolation of the velocity in the tangential directions $\mathbf{t}_1$ and $\mathbf{t}_2$. The pressure, $p_\mathbf{i}^\star$, and rigid-body body accelerations, $\mathbf{a}_b^\star$ and $\mathbf{b}_b^\star$, are then determined in Step 4, by solving a discrete Poisson equation with the AMP interface conditions. Steps 5 and 6 update the variables for the rigid body and the composite grid at t_{n+1}, and these steps are similar to the ones in the preliminary stage. The corrector stage, consisting of Steps 7–10, follows the steps in the predictor stage, and is usually applied once in order to increase the stability region of the scheme to allow a larger advection time-step. Finally, we have included an optional velocity correction in Step 11 as was done in [1, 2], which has been shown to significantly improve the numerical stability to overcome added-damping effects.

In Algorithm 1, the symbols ∇_h and Δ_h denote discrete approximations to the gradient and Laplacian operators, respectively, and these operators are implemented using standard second-order finite differences. In the implementation of the AMP interface conditions in Steps 4 and 8, the term $\Delta\mathbf{v}$ in the boundary condition (25) has been replaced by the equivalent form $-\nabla\times\nabla\times\mathbf{v}$ to improve the time-step restriction. (see [46] for more details of its effects). The interface conditions also use discrete approximations of the added-damping tensors as discussed in more detail in Section 4.2.

4. Numerical approach

4.1. Moving composite grids

The moving composite grid approach described originally in [3] within the context of inviscid, compressible flow is adapted here to handle the moving geometry in three space dimensions associated with the surfaces of the moving rigid bodies in the current FSI regime. As illustrated in Figure 2, an overlapping grid, denoted as $\mathcal{G}$, covers the entire fluid domain and consists of a set of component grids $\{G_g\}$, $g = 1, \ldots, \mathcal{N}$. In three dimensions, each component grid, G_g, is a logically rectangular, curvilinear grid defined by a smooth mapping from a unit cube parameter space $\boldsymbol{\xi}$ to physical space $\mathbf{x}$,

$$\mathbf{x} = \mathbf{G}_g(\boldsymbol{\xi}, t), \qquad \boldsymbol{\xi} \in [0,1]^3, \qquad \mathbf{x} \in \mathbb{R}^3. \tag{28}$$

All grid points in $\mathcal{G}$ are classified as discretization, interpolation or unused points. The overlapping grid generator **Ogen** [47] from the *Overture* framework of codes is used to provide this information. In a typical

Algorithm 1 Added-mass partitioned (AMP-RB) scheme

// Preliminary body evolution step

1. Predict the rigid-body degrees of freedom:
$\mathbf{a}_b^{(e)} = 2\mathbf{a}_b^n - \mathbf{a}_b^{n-1}, \quad \mathbf{b}_b^{(e)} = 2\mathbf{b}_b^n - \mathbf{b}_b^{n-1}, \quad \mathbf{v}_b^{(e)} = \mathbf{v}_b^{n-1} + 2\Delta t\,\mathbf{a}_b^n,$
$\boldsymbol{\omega}_b^{(e)} = \boldsymbol{\omega}_b^{n-1} + 2\Delta t\,\mathbf{b}_b^n, \quad \mathbf{x}_b^{(e)} = \mathbf{x}_b^{n-1} + 2\Delta t\,\mathbf{v}_b^n, \quad E_b^{(e)} = E_b^{n-1} + 2\Delta t\,\boldsymbol{\omega}_b^n \times E_b^n.$
2. Predict the moving grid $\mathcal{G}^{(e)}$ by $\mathbf{x}_b^{(e)}$ and $E_b^{(e)}$.

// Prediction steps

3. Advance the fluid velocity $\mathbf{v}_\mathbf{i}^\star$:
$$\begin{cases} \rho\Big(\mathbf{v}_\mathbf{i}^\star - \mathbf{v}_\mathbf{i}^n\Big)/\Delta t + \Big(3\mathbf{f}_\mathbf{i}^n - \mathbf{f}_\mathbf{i}^{n-1}\Big)/2 = \mu\Big(\Delta_h \mathbf{v}_\mathbf{i}^\star + \Delta_h \mathbf{v}_\mathbf{i}^n\Big)/2, & \mathbf{i} \in \Omega_h, \\ \mathbf{v}_\mathbf{i}^\star = \mathbf{v}_b^{(e)} + \boldsymbol{\omega}_b^{(e)} \times (\mathbf{r}_\mathbf{i}^{(e)} - \mathbf{x}_b^{(e)}), \quad \nabla_h \cdot \mathbf{v}_\mathbf{i}^\star = 0, \quad \text{Extrapolate ghost: } \mathbf{t}_m^T \mathbf{v}_\mathbf{i}^\star, & \mathbf{i} \in \Gamma_h, \\ \text{Velocity boundary conditions on } \partial\Omega_h \backslash \Gamma_h. \end{cases}$$
4. Update the pressure $p_\mathbf{i}^\star$ and body accelerations $\mathbf{a}_b^\star$, $\mathbf{b}_b^\star$:
$$\begin{cases} \Delta_h p_\mathbf{i}^\star = -\nabla_h \mathbf{v}_\mathbf{i}^\star : (\nabla_h \mathbf{v}_\mathbf{i}^\star)^T, & \mathbf{i} \in \Omega_h, \\ \mathbf{n}_\mathbf{i}^T \nabla_h p_\mathbf{i}^\star + \rho \mathbf{n}_\mathbf{i}^T \Big(\mathbf{a}_b^\star + \mathbf{b}_b^\star \times (\mathbf{r}_\mathbf{i}^{(e)} - \mathbf{x}_b^{(e)})\Big) = -\rho \mathbf{n}_\mathbf{i}^T \Big(\boldsymbol{\omega}_b^{(e)} \times [\boldsymbol{\omega}_b^{(e)} \times (\mathbf{r}_\mathbf{i}^{(e)} - \mathbf{x}_b^{(e)})]\Big) - \mu \mathbf{n}_\mathbf{i}^T (\nabla_h \times \nabla_h \times \mathbf{v}_\mathbf{i}^\star), & \mathbf{i} \in \Gamma_h, \\ \left\{ \begin{bmatrix} m_b\, I_{3\times 3} & 0 \\ 0 & \mathbf{I}_b \end{bmatrix} + \Delta t\, \mathbf{D}^{(e)} \right\} \begin{bmatrix} \mathbf{a}_b^\star \\ \mathbf{b}_b^\star \end{bmatrix} + \mathbf{F}(p_\mathbf{i}^\star) = - \begin{bmatrix} 0 \\ \boldsymbol{\omega}_b^{(e)} \times \mathbf{I}_b \boldsymbol{\omega}_b^{(e)} \end{bmatrix} + \mathbf{G}(\mathbf{v}_\mathbf{i}^\star) + \Delta t\, \mathbf{D}^{(e)} \begin{bmatrix} \mathbf{a}_b^{(e)} \\ \mathbf{b}_b^{(e)} \end{bmatrix}, \\ \text{Pressure boundary conditions on } \partial\Omega_h \backslash \Gamma_h. \end{cases}$$
5. Update the rigid-body degrees of freedom:
$\mathbf{v}_b^\star = \mathbf{v}_b^n + \Delta t\,(\mathbf{a}_b^\star + \mathbf{a}_b^n)/2, \quad \boldsymbol{\omega}_b^\star = \boldsymbol{\omega}_b^n + \Delta t\,(\mathbf{b}_b^\star + \mathbf{b}_b^n)/2,$
$\mathbf{x}_b^\star = \mathbf{x}_b^n + \Delta t\,(\mathbf{v}_b^\star + \mathbf{v}_b^n)/2, \quad E_b^\star = E_b^n + \Delta t\,(\boldsymbol{\omega}_b^\star \times E_b^{(e)} + \boldsymbol{\omega}_b^n \times E_b^n)/2.$
6. Update the moving grid $\mathcal{G}^\star$ by $\mathbf{x}_b^\star$ and $E_b^\star$.

// Correction steps

7. Advance the fluid velocity $\mathbf{v}_\mathbf{i}^{n+1}$:
$$\begin{cases} \rho\Big(\mathbf{v}_\mathbf{i}^{n+1} - \mathbf{v}_\mathbf{i}^n\Big)/\Delta t + \Big(\mathbf{f}_\mathbf{i}^\star + \mathbf{f}_\mathbf{i}^n\Big)/2 = \mu\Big(\Delta_h \mathbf{v}_\mathbf{i}^{n+1} + \Delta_h \mathbf{v}_\mathbf{i}^n\Big)/2, & \mathbf{i} \in \Omega_h, \\ \mathbf{v}_\mathbf{i}^{n+1} = \mathbf{v}_b^\star + \boldsymbol{\omega}_b^\star \times (\mathbf{r}_\mathbf{i}^\star - \mathbf{x}_b^\star), \quad \nabla_h \cdot \mathbf{v}_\mathbf{i}^{n+1} = 0, \quad \text{Extrapolate ghost: } \mathbf{t}_m^T \mathbf{v}_\mathbf{i}^{n+1}, & \mathbf{i} \in \Gamma_h, \\ \text{Velocity boundary conditions on } \partial\Omega_h \backslash \Gamma_h. \end{cases}$$
8. Update the pressure $p_\mathbf{i}^{n+1}$ and body accelerations $\mathbf{a}_b^{n+1}$, $\mathbf{b}_b^{n+1}$:
$$\begin{cases} \Delta_h p_\mathbf{i}^{n+1} = -\nabla_h \mathbf{v}_\mathbf{i}^{n+1} : (\nabla_h \mathbf{v}_\mathbf{i}^{n+1})^T, & \mathbf{i} \in \Omega_h, \\ \mathbf{n}_\mathbf{i}^T \nabla_h p_\mathbf{i}^{n+1} + \rho \mathbf{n}_\mathbf{i}^T \Big(\mathbf{a}_b^{n+1} + \mathbf{b}_b^{n+1} \times (\mathbf{r}_\mathbf{i}^\star - \mathbf{x}_b^\star)\Big) = -\rho \mathbf{n}_\mathbf{i}^T \Big(\boldsymbol{\omega}_b^\star \times [\boldsymbol{\omega}_b^\star \times (\mathbf{r}_\mathbf{i}^\star - \mathbf{x}_b^\star)]\Big) - \mu \mathbf{n}_\mathbf{i}^T (\nabla_h \times \nabla_h \times \mathbf{v}_\mathbf{i}^{n+1}), & \mathbf{i} \in \Gamma_h, \\ \left\{ \begin{bmatrix} m_b\, I_{3\times 3} & 0 \\ 0 & \mathbf{I}_b \end{bmatrix} + \Delta t\, \mathbf{D}^\star \right\} \begin{bmatrix} \mathbf{a}_b^{n+1} \\ \mathbf{b}_b^{n+1} \end{bmatrix} + \mathbf{F}(p_\mathbf{i}^{n+1}) = - \begin{bmatrix} 0 \\ \boldsymbol{\omega}_b^\star \times \mathbf{I}_b \boldsymbol{\omega}_b^\star \end{bmatrix} + \mathbf{G}(\mathbf{v}_\mathbf{i}^{n+1}) + \Delta t\, \mathbf{D}^\star \begin{bmatrix} \mathbf{a}_b^\star \\ \mathbf{b}_b^\star \end{bmatrix}, \\ \text{Pressure boundary conditions on } \partial\Omega_h \backslash \Gamma_h. \end{cases}$$
9. Update the rigid-body degrees of freedom:
$\mathbf{v}_b^{(n+1)} = \mathbf{v}_b^n + \Delta t\,(\mathbf{a}_b^{(n+1)} + \mathbf{a}_b^n)/2, \quad \boldsymbol{\omega}_b^{(n+1)} = \boldsymbol{\omega}_b^n + \Delta t\,(\mathbf{b}_b^{(n+1)} + \mathbf{b}_b^n)/2,$
$\mathbf{x}_b^{(n+1)} = \mathbf{x}_b^n + \Delta t\,(\mathbf{v}_b^{(n+1)} + \mathbf{v}_b^n)/2, \quad E_b^{(n+1)} = E_b^n + \Delta t\,(\boldsymbol{\omega}_b^{(n+1)} \times E_b^\star + \boldsymbol{\omega}_b^n \times E_b^n)/2.$
10. Update the moving grid $\mathcal{G}^{(n+1)}$ by $\mathbf{x}_b^{(n+1)}$ and $E_b^{(n+1)}$.

// Fluid-velocity correction step (optional)

11. Advance the fluid velocity $\mathbf{v}_\mathbf{i}^{n+1}$:
$$\begin{cases} \rho\Big(\mathbf{v}_\mathbf{i}^{n+1} - \mathbf{v}_\mathbf{i}^n\Big)/\Delta t + \Big(\mathbf{f}_\mathbf{i}^{n+1} + \mathbf{f}_\mathbf{i}^n\Big)/2 = \mu\Big(\Delta_h \mathbf{v}_\mathbf{i}^{n+1} + \Delta_h \mathbf{v}_\mathbf{i}^n\Big)/2, & \mathbf{i} \in \Omega_h, \\ \mathbf{v}_\mathbf{i}^{n+1} = \mathbf{v}_b^{n+1} + \boldsymbol{\omega}_b^{n+1} \times (\mathbf{r}_\mathbf{i}^{n+1} - \mathbf{x}_b^{n+1}), \quad \nabla_h \cdot \mathbf{v}_\mathbf{i}^{n+1} = 0, \quad \text{Extrapolate ghost: } \mathbf{t}_m^T \mathbf{v}_\mathbf{i}^{n+1}, & \mathbf{i} \in \Gamma_h, \\ \text{Velocity boundary conditions on } \partial\Omega_h \backslash \Gamma_h. \end{cases}$$

composite grid for the current FSI application, one or more boundary-fitted curvilinear grids in the fluid are used to represent the surface of each rigid body. These grids move with the body according to its computed location information $\mathbf{x}_b(t)$ and $E_b(t)$ following the formulas in (12) and (13). The remainder of the fluid domain is covered by one or more static Cartesian grids. **Ogen** cuts holes in the appropriate component grids by locating the physical boundary, which includes the interface between the rigid bodies and the fluid, and thus determines the unused points based on their location. For instance, the "cylinder" grid displayed in the upper right image of Figure 2 cuts a hole in the Cartesian "box" grid so that the

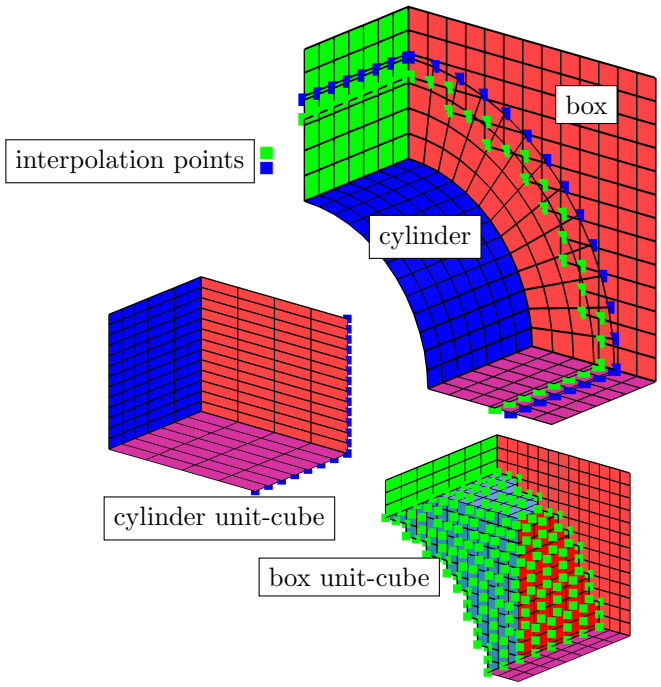

Figure 2: Top: a three-dimensional overlapping grid for a quarter-cylinder in a box. Bottom left and right: component grids for the cylindrical and box grids in the unit cube parameter space. Interpolation points at the grid overlap are marked and color-coded for each component grid.

latter grid has many unused points (those not being plotted in the lower right image). **Ogen** also provides the interpolation information for all interpolation points in the overlap region between component grids. Two types of interpolation, called *explicit* and *implicit*, are supported in **Ogen** and both types are used in the current work. For explicit interpolation, the grid points used in the interpolation stencil of each donor component grid must be discretization points. The solution values at interpolation points for explicit interpolation are thus computed explicitly from the values at discretization points on the donor grids. In contrast, the grid points needed on donor component grids for implicit interpolation may themselves be interpolation points, and thus the solution values at interpolation points are coupled between component grids and must be computed implicitly. Explicit interpolation is typically used in our simulations because of its faster overall performance. However, wider overlaps between component grids are needed for explicit interpolation, and thus for some difficult problems, especially when the grids are relatively coarse, implicit interpolation is more robust in producing valid composite grids. For example, the coarsest grids in the calculations of the settling particle and three-dimensional heart valve use implicit interpolation. Further discussion of issues related to three-dimensional composite grids can be found in [38]. On discretization points of each component grid, the equations governing the fluid are discretized with second-order accurate approximations on the unit cube parameter space following an exact transformation of the equations using the metrics of the known mapping in (28). See [3, 38, 45] for more details on the discretization approach on overlapping grids.

4.2. Computing surface integrals on composite grids

The computation of the forces and torques on the body (27) as well as the evaluation of discrete approximations to the exact added damping tensors (20) requires discrete approximations to integrals over the surface of the rigid body. This surface quadrature must account for regions on the surface covered by all boundary-fitted component grids, and must avoid over counting where two or more component grids overlap. One common way to avoid the over counting issue is to construct an unstructured surface triangulation in the areas of overlap [48]. The solution from the overlapping grid can be interpolated to the vertices or cell centers of the surface triangles from which a discrete surface integral can be defined. In this paper we use

an alternative approach to find the surface quadrature that does not require a surface triangulation[5]. The approach is based on the fact that the Neumann problem

$$\Delta\phi = f, \quad \mathbf{x} \in \Omega, \tag{29a}$$

$$\frac{\partial\phi}{\partial n} = g \quad \mathbf{x} \in \partial\Omega, \tag{29b}$$

only has a solution (and that solution is determined up to an additive constant) when

$$\iiint_\Omega f(\mathbf{x})\, dV = \int_{\partial\Omega} g(\mathbf{x})\, dS. \tag{30}$$

Similarly a discrete approximation to (29) on an overlapping (or non-overlapping) grid,

$$A\boldsymbol{\phi} = \mathbf{f}$$

only has a solution when

$$\mathbf{w}^T\mathbf{f} = 0, \tag{31}$$

where $\mathbf{w}$ is the left null vector of A, $\mathbf{w}^T A = 0$. (As before the solution is determined up to an additive constant.) The constraint in (31) is a discrete counter-part of the integral constraint in (30), and thus $\mathbf{w}$ holds the coefficients of a discrete approximation to the volume and surface integrals in (30). To determine these coefficients, $\mathbf{w}$ must be scaled by an appropriate constant, and this constant can be determined by matching the coefficients in $\mathbf{w}$ to the expected quadrature weights in regions away from the overlap. We note that the quadrature weights need only be computed once at the start of the simulation in view of the transformation in (22).

4.3. Parallel implementation and performance

Both serial and parallel versions of the three-dimensional AMP-RB time-stepping scheme have been implemented based on the incompressible Navier-Stokes solver **Cgins** [51] within the *Overture* framework. The parallel version of the code follows the work in [38, 52], and is based on a domain-decomposition approach in which each component grid G_g is partitioned across different processors of a distributed-memory parallel computer. The component grids are partitioned using a load-balancing algorithm that depends on the number of the grid points on each grid and the number of processors available. In the current FSI application, the static background Cartesian grids contain the majority of the grid points in each simulation, and these grids are generally partitioned across all of the available processors. The boundary-fitted grids are usually narrow in the direction normal to the surface of the rigid bodies and so these grids contain a relatively small number of grid points. As a result, these narrow grids are usually partitioned across a subset of the available processors, or may even reside on a single processor. For more details on the parallel implementation of PDE solvers on overlapping grids, see [38, 52].

In the present work, special attention has been given to the implementation of the AMP-RB interface conditions in parallel. These conditions provide additional boundary conditions for the pressure Poisson equation in Steps 4 and 8 of Algorithm 1. The extra equations due to the interface conditions have the same number as the degrees of freedom for the rigid bodies, and these equations are appended to the end of the linear system for the pressure equation. In our implementation, the extra equations reside in the last available processor in the parallel sparse linear solver. However, the grid points corresponding to the entries of $\mathbf{F}(p)$ in (27) may reside over several processors in general and this requires some communication across processors. This communication is very fast as compared to the linear solver since the surface integrals in $\mathbf{F}(p)$ are one dimension lower than the full three dimensions of the FSI problem. All of the parallel communication, including the communication for the interface conditions, are performed using the Message Passing Interface (MPI).

[5]This approach was discovered by one of the authors in the course of forming conservative approximations for composite grids [49, 50].

All linear systems in the AMP-RB scheme are solved in parallel using the Krylov methods available in the PETSc library [53]. These linear systems include the implicit equations for the fluid velocity in Steps 3 and 7 (and optionally Step 11) of Algorithm 1 as well as the aforementioned pressure Poisson equations. The stabilized bi-conjugate-gradient (Bi-CGSTAB) method with a block-Jacobi preconditioning is used for most of the simulations with an incomplete LU (ILU) preconditioner for each individual block. The velocity equation uses ILU(1) as the preconditioner, while the pressure equation uses ILU(1) for easy problems and ILU(3) for some hard problem that require 20 to 50 iterations to converge. We found that these choices give the best performance amongst the Krylov solvers tested. For one three-dimensional heart valve simulation, the parallel Bi-CGSTAB solver failed to converge in the first pressure solve, presumably from a poor initial guess. For this case, a parallel GMRES solver was used for a few time steps before switching back to the Bi-CGSTAB solver for improved efficiency.

Figure 3 presents the parallel performance of the AMP-RB scheme on a distributed memory Linux cluster with 2.5 GHz Xeon processors. The figure gives strong scaling results for the settling-particle problem described later in Section 5.2 using a sphere-in-a-box grid with 1.3×10^7 grid points. The graph and the CPU time table show that the parallel scaling is reasonable up to 16 processors. The breakdown of the CPU times in the table shows that most of the computational cost is used in the Krylov solves of the pressure and velocity equations, and thus the parallel performance depends heavily on the scaling of the Krylov solvers for this problem. We note that the computational domain for this problem is relatively simple, and hence the **Ogen** grid generator is very efficient and scales well in parallel. However, the grid generator has not yet been optimized for moving grid problems and can be more costly for complex problems. For example, it has been observed that the grid generator can use up to half of the computational cost for the heart valve simulations described later in Section 5.5.2.

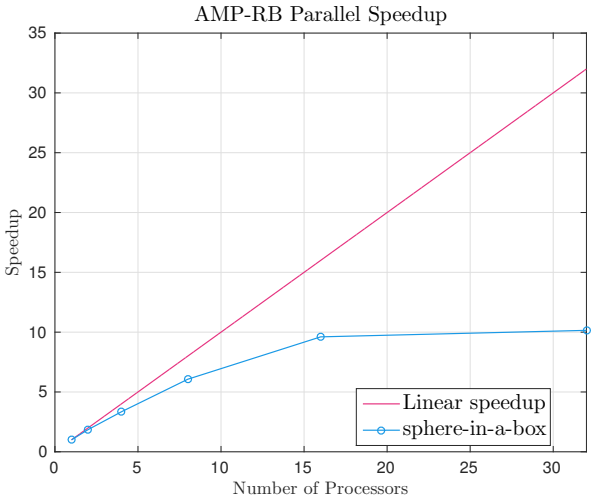

Parallel results for a sphere-in-a-box grid						
	1 precessor		4 processors		16 processors	
	s/step	%	s/step	%	s/step	%
grid	18	3.3	5	3.0	2	3.2
psolver	305	56.7	95	59.4	33	58.7
vsolver	185	34.4	52	32.7	19	33.2
others	30	5.6	9	4.9	2	4.9
total	538	100	161	100	56	100

Figure 3: Left: strong scaling results for the sphere-in-a-box grid with approximately 13 million grid points. Right: CPU time (in seconds) for various parts of the AMP-RB scheme, and their percentages of the total CPU time per step. "Grid" stands for the moving composite grid generator, while "psolver" and "vsolver" for the Krylov solvers for the pressure and velocity respectively. The results of 1, 4 and 16 processors are presented.

5. Numerical results

Several benchmark problems are considered in this section to demonstrate the stability and accuracy of the AMP-RB scheme. We begin in Section 5.1 by revisiting the one-dimensional motion of a piston in a fluid chamber discussed in [1, 2]. Here, we solve the problem using the AMP-RB scheme for a three-dimensional fluid chamber and compare the numerical results with the exact solution. This benchmark problem provides a good first test of both the accuracy of the scheme as well as its added-mass stability properties. In Section 5.2, we consider a second benchmark problem involving the settling of a moderately

light particle in a small container. For this problem, the numerical solution given by the AMP-RB scheme is compared with experimental data and with other numerical results from the literature, and a self-convergence study is conducted to demonstrate the accuracy of the scheme. We also use this second problem to study the added-damping stability properties of the AMP-RB scheme. Section 5.3 is devoted to a comparison of the AMP-RB scheme and a traditional partitioned (TP-RB) scheme, which is performed using the previous settling particle problem. Both schemes require the solution of a Poisson problem for the pressure at each time step. The pressure solve for the TP-RB scheme uses a boundary condition for the pressure alone whereas the AMP-RB scheme uses interface conditions involving the pressure and the accelerations of the rigid body. The corresponding linear systems are different but have similar conditioning. We are also interested in a comparison of the performance of the two schemes, and this demonstrates the efficiency of the present scheme. In Section 5.4, a third benchmark problem involving a particle rising or falling in a long container is considered. The numerical solution given by the AMP-RB scheme is compared with the results of various algorithms discussed in the literature. Importantly, this problem is used to confirm that the AMP-RB scheme is stable for rigid-body FSI problems involving different density ratios of the solid bodies and the fluid, including the difficult case of a body with small, or even zero, mass. This difficult case has proved to be challenging, or impossible, for other available schemes due to the severe added-mass instability. The last problem we consider is an FSI problem generalized from a bi-leaflet mechanical heart valve. Simulations of this problem in two dimensions (Section 5.5.1) and three dimensions (Section 5.5.2) are discussed. For this application, two leaflets are hinged and allowed to rotate along the hinge axes. An oscillating pressure gradient is applied to drive a fluid flow through the value, and repulsive torques and damping terms are implemented to restrict the rotation of the leaflets to the designed range. This example demonstrates the behavior of the AMP-RB scheme when multiple light bodies are involved, and further confirms that the numerical instabilities have been suppressed in the present scheme for such cases.

5.1. One-dimensitonal motion of a piston

In this section, we consider the piston problem discussed previously in [1, 2], but extended here to three space dimensions. In this problem a rigid body is adjacent to one end of a fluid channel with rectangular cross section. Two problems were considered previously, one in which the body moved normal to the channel and the other where the body moves tangentially, and exact solutions were found for each case. Here, we focus on the problem from [2] in which the body moves normal to the channel, and we use this problem to verify the stability and accuracy of the AMP-RB scheme. Unlike the previous test of the two-dimensional version of the scheme where a single body-fitted rectangular grid is used to represent the surface of the body, the current test uses multiple body-fitted component grids to verify the implementation and accuracy of the calculation of surface integrals on the body for a case when the body-fitted grids overlap.

For this problem, a rectangular rigid body of size $L_b \times H \times W$ and mass m_b is adjacent to the fluid domain, $\Omega(t) = [x_I(t), L] \times [0, H] \times [0, W]$, where $x = x_I(t)$ is the body-fitted end of the fluid channel. The fluid in the channel is governed by the incompressible Navier-Stokes equations with a density and viscosity taken to be $\rho = 1$ and $\mu = 0.1$, respectively. The boundary conditions on the fluid at the fixed end of the channel, $x = L$, are

$$p(L, y, z, t) = p_L(t), \qquad v_2(L, y, z, t) = v_3(L, y, z, t) = 0, \qquad (y, z) \in [0, H] \times [0, W], \quad t > 0,$$

where $p_L(t)$ is an applied pressure to be determined. The velocity matching condition in (11) is applied at $x = x_I(t)$, and slip-wall boundary conditions are applied on the remaining four sides of the fluid channel. Exact solutions for the velocities of the body, $\mathbf{v}_b = (v_{1,b}, v_{2,b}, v_{3,b})^T$, and fluid, $\mathbf{v} = (v_1, v_2, v_3)^T$, and for the fluid pressure p have the form

$$v_{1,b}(t) = \int_0^t \frac{-HW p_L(\tau)\, d\tau}{m_b + M_a(\tau)} + v_{1,b}(0), \tag{32}$$

$$p(x, t) = p_L(t) + \left(\frac{L - x}{L - x_I(t)}\right) \frac{-p_L(t)}{m_b/M_a(t) + 1}, \tag{33}$$

$$v_1(t) = v_{1,b}(t), \tag{34}$$

and $v_2 = v_3 = v_{2,b} = v_{3,b} = 0$. The *added-mass* for this problem found analytically in [2] to be

$$M_a(t) = \rho HW\big(L - x_I(t)\big). \tag{35}$$

Because the horizontal velocity is $v_{1,b}(t)$, the horizontal position is calculated as

$$x_b(t) = \int_0^t v_{1,b}(\tau)\, d\tau + x_b(0). \tag{36}$$

The applied pressure at the fixed end of the channel given by $p_L(t)$ can be specified by choosing a motion for the rigid body. For the present tests, we take x_b to be

$$x_b(t) = \alpha_b \sin(2\pi t), \qquad \alpha_b = 1/4, \tag{37}$$

which is sufficient to specify the exact solution.

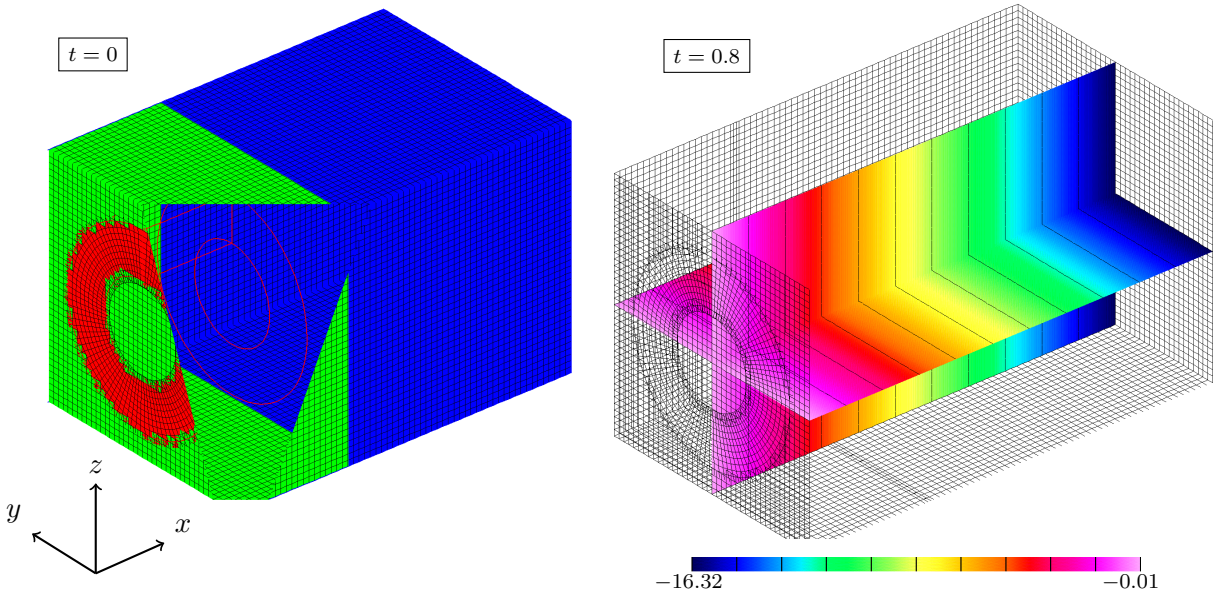

Figure 4: Left: Composite grids $\mathcal{G}_p^{(4)}$ for a piston adjacent to a fluid channel at $t = 0$. The piston is initially located at $x = 0$ and adjacent to the left end of the fluid grid. The green Cartesian grid and the red curvilinear grid adjacent to the piston move in time. The blue background grid remains fixed. Right: Computed pressure and the grid $\mathcal{G}_p^{(4)}$ at $t = 0.8$.

Numerical solutions are computed using a composite grid, denoted by $\mathcal{G}_p^{(j)}$, with resolution factor j, as shown in Figure 4. The composite grid consists of three component grids, the first of which is a body-fitted Cartesian grid (green in the figure) of fixed length $1/2$ in x-direction, and of width $W = 1$ and height $H = 1$ in y and z-directions, respectively. Inside this first body-fitted grid, there is an extra body-fitted cylindrical grid (red in the figure) of fixed length equal to 0.4 in the x-direction, and with inner radius 0.2 and outer radius 0.4. These two body-fitted grids overlap and move in time as the body moves. Note that the cylindrical grid is not needed to handle the geometry of the problem, but is intentionally added to test the calculation of surface integrals on the body as discussed in Section 4.2. In addition to these body-fitted grids, there is a static Cartesian background grid (blue in the figure) covering the domain $[-3/4, L] \times [0, H] \times [0, W]$ with $L = 3/2$. The approximate grid spacing for all of the grids is $h^{(j)} = 1/(10j)$ in each of their coordinate directions. The length of the rigid body is chosen to be $L_b = 1$ and hence $m_b = \rho_b$, which will be varied in different cases. Figure 4 also shows the computed pressure at $t = 0.8$ (using $\Delta t = 0.01$) for the case of a very light body with $\rho_b = 0.001$ along with a wire frame of parts the composite grid $\mathcal{G}_p^{(4)}$.

As a test, the AMP-RB scheme has been run for this piston problem using $\mathcal{G}_p^{(4)}$ and $\Delta t = 0.01$ for a wide range of densities of the body, from very light ($\rho_b = 10^{-7}$) to very heavy ($\rho_b = 10^7$), and for all cases we observe that the scheme remains stable and gives accurate results. For example, the time history of the position, velocity and acceleration of the rigid body, as well as their errors, are presented in Figure 5 for a medium-weight body with $\rho_b = 1$ (colored curves) and a very light body $\rho_b = 0.001$ (black curves). These results illustrate the stability and accuracy of the simulations. As a comparison, we have also used the TP-RB scheme without sub-timestep-iterations to compute numerical solutions of this problem and have found

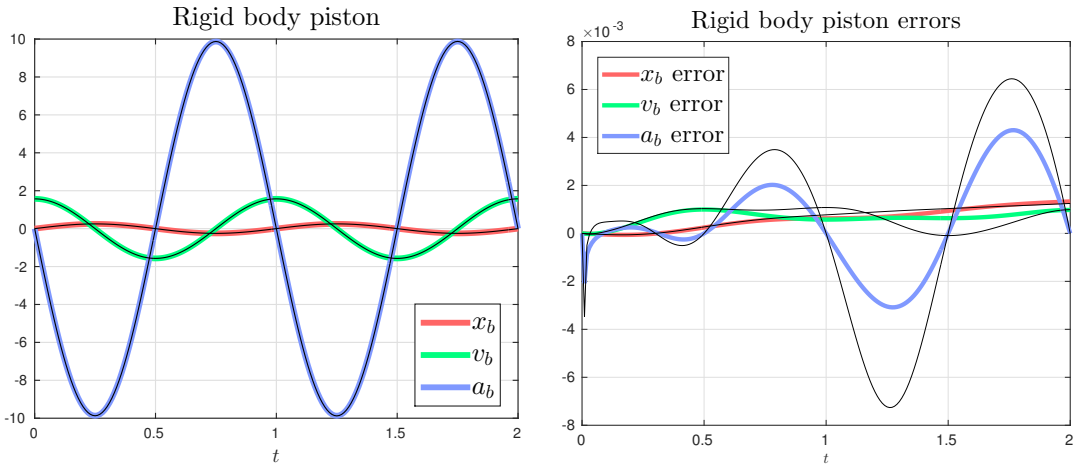

Figure 5: Computed piston motion and errors for $\rho_b = 1$ (colored lines) and $\rho_b = 0.001$ (black lines). The solutions are computed on grid $\mathcal{G}_p^{(4)}$.

that it is unstable for calculations using $\mathcal{G}_p^{(4)}$ and $\Delta t = 0.01$ if $\rho_b = m_b \approx 2.0$ or smaller. This observation is in reasonable agreement with the stability results in [1, 2], where additional details are discussed.

Piston motion, $\rho_b = 10$										
$h^{(j)}$	E_j^p	r	$E_j^{\mathbf{v}}$	r	$E_j^{\mathbf{x}_b}$	r	$E_j^{\mathbf{v}_b}$	r	$E_j^{\mathbf{a}_b}$	r
1/10	1.4e-2		6.9e-3		9.2e-3		6.9e-3		7.5e-3	
1/20	3.2e-3	4.3	1.7e-3	4.1	2.3e-3	4.0	1.7e-3	4.1	1.8e-3	4.1
1/40	8.1e-4	4.0	4.5e-4	3.8	5.6e-4	4.0	4.2e-4	4.0	4.5e-4	4.0
rate	2.04		1.97		2.01		2.02		2.02	

Piston motion, $\rho_b = 1$										
$h^{(j)}$	E_j^p	r	$E_j^{\mathbf{v}}$	r	$E_j^{\mathbf{x}_b}$	r	$E_j^{\mathbf{v}_b}$	r	$E_j^{\mathbf{a}_b}$	r
1/10	5.9e-2		1.2e-2		9.6e-3		1.2e-2		3.4e-2	
1/20	1.4e-2	4.2	2.8e-3	4.2	2.4e-3	4.1	2.8e-3	4.2	8.1e-3	4.2
1/40	3.5e-3	4.1	6.9e-4	4.0	5.8e-4	4.0	6.9e-4	4.1	2.0e-3	4.1
rate	2.04		2.04		2.02		2.04		2.04	

Piston motion, $\rho_b = 0.001$										
$h^{(j)}$	E_j^p	r	$E_j^{\mathbf{v}}$	r	$E_j^{\mathbf{x}_b}$	r	$E_j^{\mathbf{v}_b}$	r	$E_j^{\mathbf{a}_b}$	r
1/10	9.9e-2		1.7e-2		1.0e-2		1.6e-2		5.8e-2	
1/20	2.4e-2	4.1	4.0e-3	4.1	2.6e-3	4.0	4.0e-3	4.1	1.4e-2	4.1
1/40	6.0e-3	4.0	9.8e-4	4.0	6.4e-4	4.0	9.8e-4	4.0	3.5e-3	4.0
rate	2.02		2.03		2.00		2.02		2.03	

Table 1: Piston motion in three dimensions. Maximum errors and estimated convergence rates at $t = 0.8$ computed using the AMP-RB scheme for a heavy, $\rho_b = 10$, medium, $\rho_b = 1$, and very light, $\rho_b = 0.001$, moving piston. The column labeled "r" provides the ratio of the errors at the current grid spacing to that on the next coarser grid.

A refinement study is conducted on a sequence of grids of increasing resolution to check the accuracy of the implementation of the AMP-RB scheme for three dimensions. The time-step is taken as $\Delta t_j = 0.4/(10j)$ for the composite grid $\mathcal{G}_p^{(j)}$, and the equations are integrated to $t_{\text{final}} = 0.8$. Note the time step is smaller than the refinement study conducted in [2] due to the stability constraint from the additional cylindrical grid which has cells with smaller volumes. However, the numerical solutions still exhibit superconvergence at $t = n/2$, where n is a nonnegative integer, corresponding to the half-period of the oscillatory motion of the body specified in (37) when $x_b = a_b = 0$, which is the case found in [2] at $t_{\text{final}} = 1$. Therefore, to avoid this superconvergence, the equations in the current study are integrated to $t_{\text{final}} = 0.8$ instead. Table 1

presents the max-norm errors and estimated convergence rates of the refinement study for a heavy, medium and light body. The max-norm error of a quantity q is denoted by E_j^q for the results on grid $\mathcal{G}_p^{(j)}$, and if q is a vector, then the maximum is taken over all of its components. The results of the table show approximately second-order accuracy for all solution quantities and for all three densities of the body. As an added check, the calculations were also performed without the extra cylindrical body-fitted grid and the errors were found to be nearly identical to the errors given in the table. This verifies the accuracy of the discrete surface integrals when computing the fluid force on the rigid body.

5.2. One particle settling in a box

We consider the common benchmark problem of a moderately light spherical particle settling due to gravity in a small container. This problem was first studied experimentally [54] by considering a spherical particle settling in silicon oil towards the bottom of a box, and it has later been widely used as a test problem to validate numerical FSI algorithms, including [8, 17, 20, 27]. The setup of the problem is as follows. A spherical particle of density $\tilde{\rho}_b = 1120$ kg/m^3 and diameter $D_b = 2\,R_b = 15$ mm is immersed in a fluid channel of a rectangular box. The fluid density is $\tilde{\rho} = 970$ kg/m^3 and its viscosity is $\tilde{\mu} = 0.373$ kg/(m s). Initially the fluid and particle are quiescent, and at $t = 0$ the particle is allowed to move under the influence of gravity as specified by the external body force,

$$\mathbf{f}_e(t) = \frac{4}{3}\pi {R_b}^3(\rho_b - \rho)\,\mathbf{g}, \tag{38}$$

where the acceleration is $\mathbf{g} = [0,\ 0,\ -\tilde{g}]$ with $\tilde{g} = 9.81$ m/s^2. In the previous studies, the problem is typically presented in terms of dimensional units. Here we prefer to nondimensionalise the problem by introducing suitable reference scales. The reference scale for length is the diameter of the particle $\tilde{d} = D_b$. The reference velocity is taken to be $\tilde{v}_{\text{term}} = 0.038$ m/s given in the original work [54], which is the terminal velocity of the particle in an infinitely long channel with the corrections due to the side boundary effects. The densities are all scaled by the fluid density of $\tilde{\rho}$. The dimensionless fluid density is therefore $\rho = 1$ and the body density is $\rho_b = 1120/970 \approx 1.1546$. The dimensionless fluid viscosity is hence $\mu = \tilde{\mu}/(\tilde{\rho}\,\tilde{d}\,\tilde{v}_{\text{term}}) = 0.67462$, corresponding to the Reynolds number $\text{Re} = 1.5$. The dimensionless gravity is $g = \tilde{g}\,\tilde{d}/(\tilde{v}_{\text{term}})^2 = 101.90$, which is turned on instantaneously at $t = 0$ in the simulation. The resulting fluid domain is $\Omega(t) = [-x_c, x_c] \times [-y_c, y_c] \times [z_0, z_1]$, with $x_c = y_c = 10/3$, $z_0 = 0$ and $z_1 = 32/3$. The particle of radius 0.5 is initially located at $(x, y, z) = (0, 0, 8.5)$. The top boundary condition of the fluid domain is a zero pressure condition, and the remaining boundary conditions are no-slip walls.

Numerical solutions are computed using a *sphere-in-a-box* composite grid, denoted by $\mathcal{G}_{\text{sp}}^{(j)}$, which consists of a background Cartesian grid and two body-fitted grids attached to the surface of the rigid body. The target background grid spacing $h^{(j)}$ is set to be $2/(15j)$, corresponding to the grid size of $(50j)\times(50j)\times(80j)$ covering the entire domain. The boundary-fitted grids are two curvilinear grids surrounding the particle, each of which covers more than half of its surface. The thin body-fitted grids have a target grid spacing approximately equal to $0.71h^{(j)}$ with a radial width of $5h^{(j)}$. The time step $\Delta t^{(j)}$ is taken as $1/(40j)$. The interested reader is referred to [38] for more details on the construction of the sphere-in-a-box grid.

The added-damping tensors for this problem are computed based on a discrete surface integral on the two body-fitted grids at the beginning of the simulation. Formulas for the discrete added-damping tensors corresponding to the exact forms in (20) for a spherical particle of radius r are given in the appendix of [2] as

$$\tilde{\mathcal{D}}^{vv} = \frac{\mu}{\Delta n}\frac{8}{3}\pi r^2 \begin{bmatrix} 1 & 0 & 0 \\ 0 & 1 & 0 \\ 0 & 0 & 1 \end{bmatrix}, \quad \tilde{\mathcal{D}}^{v\omega} = \mathbf{0}, \quad \tilde{\mathcal{D}}^{\omega\omega} = \frac{\mu}{\Delta n}\frac{8}{3}\pi r^4 \begin{bmatrix} 1 & 0 & 0 \\ 0 & 1 & 0 \\ 0 & 0 & 1 \end{bmatrix}.$$

where

$$\Delta n \stackrel{\text{def}}{=} \frac{\Delta s_n}{1 - e^{-\delta}}, \qquad \delta \stackrel{\text{def}}{=} \frac{\Delta s_n}{\sqrt{\nu \Delta t/2}}, \tag{39}$$

with Δs_n being the mesh spacing in the normal direction, i.e. $\Delta s_n \approx 0.71h^{(j)}$ for the present calculations. Here, $r = 0.5$ so that the diagonal elements of the added-damping tensors are

$$\tilde{\mathcal{D}}_{ii}^{vv} = \frac{8}{3}\pi r^2 \frac{\mu}{\Delta n} \approx 2.0944\,\frac{\mu}{\Delta n}, \qquad \tilde{\mathcal{D}}_{ii}^{\omega\omega} = \frac{8}{3}\pi r^4 \frac{\mu}{\Delta n} \approx 0.52360\,\frac{\mu}{\Delta n}, \qquad i = 1, 2, 3,$$

which is in excellent agreement with the values computed by the discrete surface integral. For instance, the diagonal elements of the tensors for the grid $\mathcal{G}_{\rm sp}^{(4)}$ are computed in the beginning of the simulation as

$$\tilde{\mathcal{D}}_{h,ii}^{vv} \approx 2.0886\,\frac{\mu}{\Delta n}, \qquad \tilde{\mathcal{D}}_{h,ii}^{\omega\omega} \approx 0.52215\,\frac{\mu}{\Delta n}, \qquad i = 1, 2, 3.$$

The off-diagonal elements are zero for the exact tensors, and this is in excellent agreement with the computed tensors for which the maximum off-diagonal element is approximately 7.3×10^{-6} in absolute value.

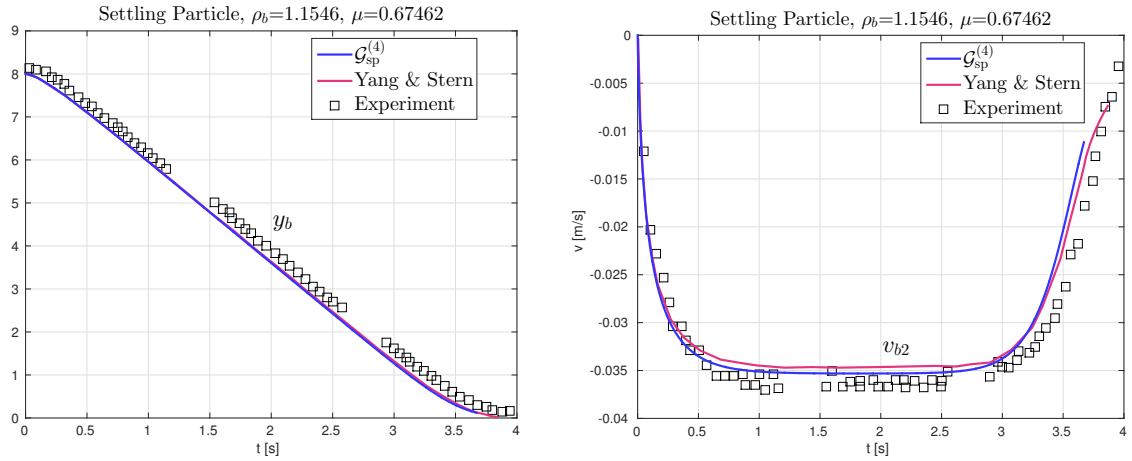

Figure 6: Settling particle. Time history of the position (left) and velocity (right). The solutions are computed on grid $\mathcal{G}_{\rm sp}^{(4)}$. The black square is the experimental data taken from Fig. 5 in [54] and the red curve is the numerical solutions taken from Fig. 13 in [20].

Figure 6 presents the time history of the vertical position, $y_b(t)$, and vertical velocity, $v_{b2}(t)$, of the body computed using the AMP-RB scheme with the composite grid $\mathcal{G}_{\rm sp}^{(4)}$. To compare with the available data, the time and velocity in Figure 6 have been scaled properly so that their units are s and m/s, respectively. The present results are in good agreement with the experimental data in [54] and the numerical results in [8, 17, 20, 27]. The numerical solutions from [20], for example, are also plotted in Figure 6 for comparison. The numerical solutions are taken directly from Fig. 5 in [20], although the velocity therein was plotted in a larger scale, which may lead to potential errors in reproducing the data. Despite these potential errors, the numerical solution of the AMP-RB scheme appears to be in good agreement with the results in [20]. It is also found that the results of the AMP-RB scheme are almost indistinguishable with the results given by the TP-RB scheme in [27]. The contours of the pressure and speed are presented in Figure 7 for three different times. The body accelerates initially due to its negative buoyancy which is turned on impulsively at $t = 0$. It then approaches a steady velocity before the body eventually slows down as it approaches the bottom wall. As in the previous work [20, 27], collisions between the particle and the wall are not considered. Therefore, the simulation is stopped when there are insufficient grid lines in the gap between the particle and the bottom wall. Note that the other three cases from [27] with difference Reynolds numbers have also been computed using the AMP-RB scheme, and it has been found that the results are almost identical to the TP-RB scheme if the same grids are used.

Figure 8 presents the behaviour of the vertical position, velocity and acceleration of the particle versus time for different grid resolutions. The numerical solutions in Figure 8 are very smooth and show good convergence as the grid resolution increases. In fact, Richardson extrapolation estimates for the convergence rate of the position and velocity are both around 1.90 at the times $t = 2$, 4 and 6. However, it is found that the resulting particle tends to drop faster at lower resolutions, and so the simulations are halted earlier (e.g., the calculation for grid $\mathcal{G}_{\rm sp}^{(1)}$ is stopped at $t \approx 7.5$). This makes the self-convergence studies challenging at the later times. Self-convergence studies of the accelerations are not as clean and yield a convergence rate of approximately 1.52 at $t = 2$ and 4, while the rate improves slightly to 1.65 at $t = 6$. There are at least two plausible reasons leading to this reduced convergence rate. One reason is that a very large gravity is turned on impulsively in this test. Due to a sudden change of the body acceleration, the first time step

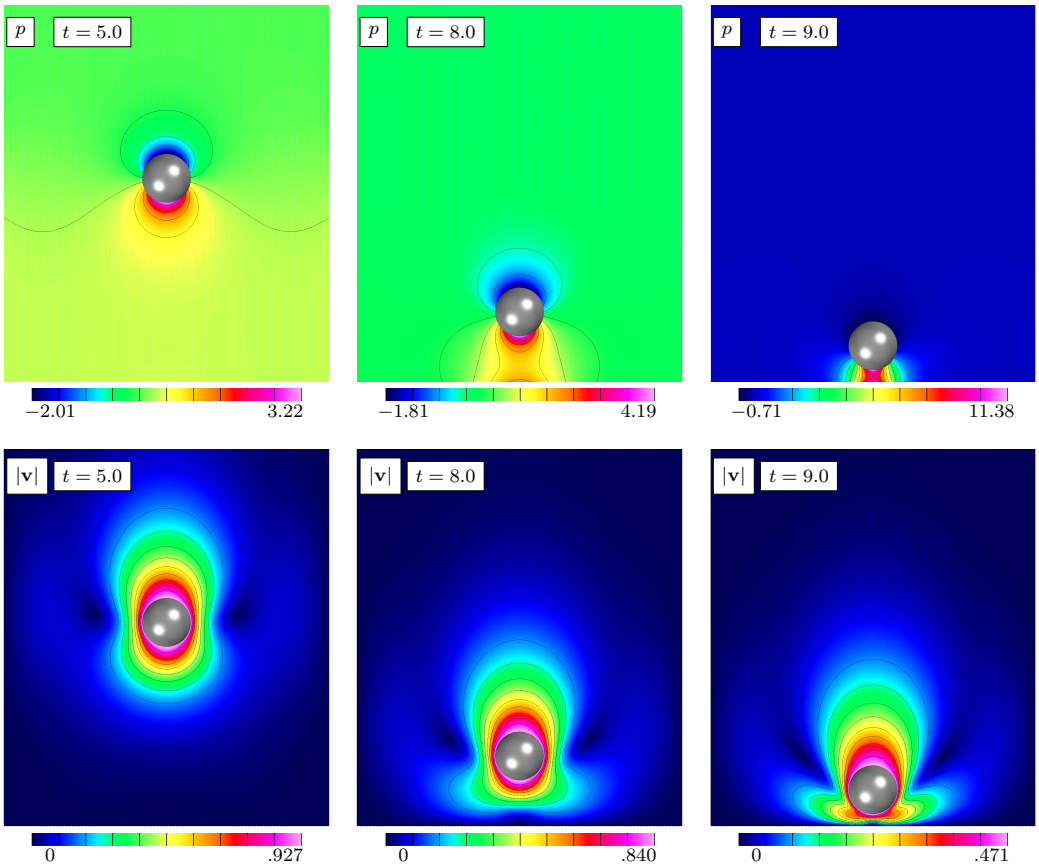

Figure 7: Settling particle. Contours of the pressure (top row) and speed (bottom row) at times $t = 5$, 8 and 9 computed using the composite grid $\mathcal{G}_{\rm sp}^{(4)}$.

may involve a first-order error, and in fact we observe that the accelerations oscillate slighlty during the first few time steps. The second reason is that the problem becomes steady during most of the simulation. This makes it more challenging for the iterative Krylov solvers used here, since the solvers may take less Krylov iterations than required to obtain the designed order of accuracy. Note that all of the tests we considered in the previous work [2] were solved by a direct sparse matrix solver, which eliminates this potential issue.

This test is further used to demonstrate the importance of including the added-damping tensors in the AMP-RB scheme. It is found that instabilities due to added-damping effects are still important for this problem even though the body density is heavier than that of the fluid and the motion of the body is primarily translational. To illustrate the importance of these tensors, Figure 9 presents the results from the AMP-RB scheme but with the added-damping tensors intentionally turned off. It is found that the particle starts to develop an unphysical rotation around $t = 0.4$, and the unphysical rotation eventually pollutes the overall motion of the particle. Different from the rising body case in [2], the counter-acting effects of the pressure is not very strong in the current test due to its geometry and the oscillations do not saturate as time evolves.

5.3. Performance comparisons between AMP-RB and TP-RB schemes

We now use the benchmark problem described in the previous section to compare several aspects of the performance of the AMP-RB and TP-RB schemes. To eliminate the complexity due to the parallel implementation, the comparisons are performed using the serial implementations of the algorithms. The main modification for the AMP-RB scheme is the application of the AMP interface conditions for the pressure Poisson equation, and so we first compare the corresponding linear system from the AMP-RB scheme to that for the TP-RB scheme. Without loss of generality, we consider the two linear systems at $t = 0$ when

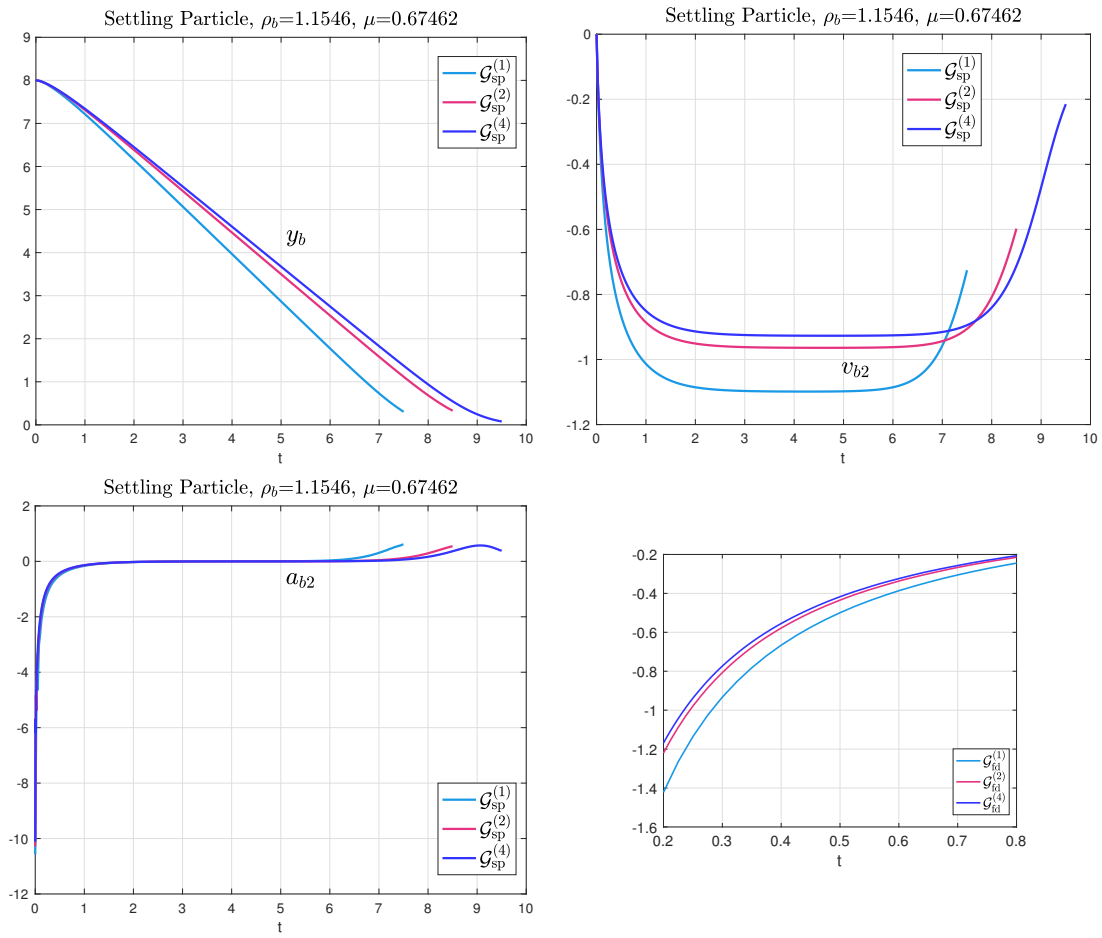

Figure 8: Settling particle. Time history of the position (top left), velocity (top right), acceleration (bottom left) and its zoomed view of the particle.

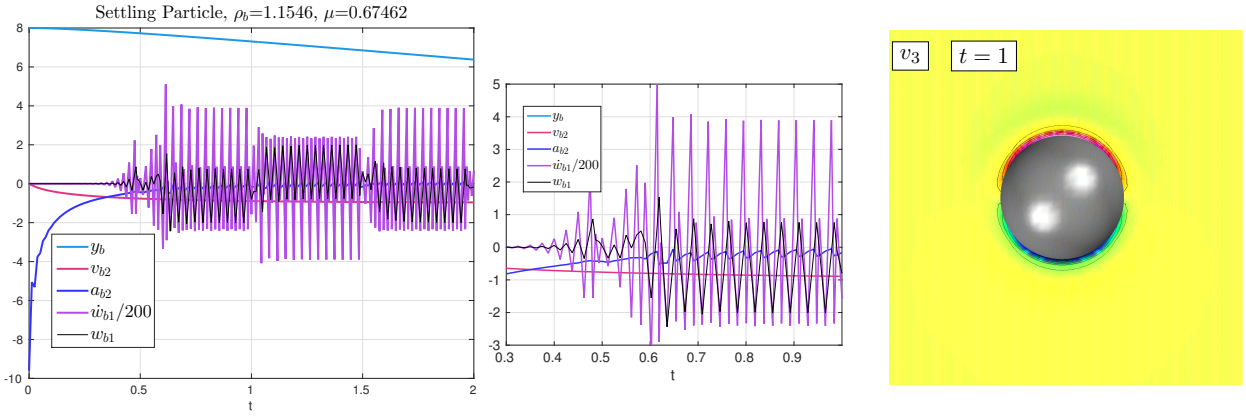

Figure 9: Illustration of the added-damping instability for the settling particle test when the added-damping tensor is turned off. The particle starts to develop an unphysical rotation around $t = 0.4$. These oscillations in the angular acceleration starts to affect the translational acceleration at $t = 0.6$, and eventually dominate the overall motion of the particle. The right plot is the contour plot of v_3 at $t = 1$, which shows the fluid velocity has been affected by the particle rotation. Results are shown for grid $\mathcal{G}_{\rm sp}^{(2)}$ solved by the AMP-RB scheme with the added-damping term turned off intentionally.

there is an impulsive gravity applied to the particle in the quiescent fluid. For this special case when $\mathbf{v} = \mathbf{0}$, the discrete Poisson problem for the AMP-RB scheme becomes

$$\Delta_h p_{\mathbf{i}} = 0, \qquad \mathbf{i} \in \Omega_h \cup \Gamma_h, \tag{40}$$

with

$$\mathbf{n}_{\mathbf{i}}^T \nabla_h p_{\mathbf{i}} + \rho \mathbf{n}_{\mathbf{i}}^T \Big(\mathbf{a}_b + \mathbf{b}_b \times (\mathbf{r}_{\mathbf{i}}^0 - \mathbf{x}_b^0) \Big) = 0, \qquad \mathbf{i} \in \Gamma_h, \tag{41}$$

$$\left\{ \begin{bmatrix} m_b\, I_{3\times 3} & 0 \\ 0 & \mathbf{I}_b \end{bmatrix} + \Delta t\, \mathbf{D}^0 \right\} \begin{bmatrix} \mathbf{a}_b \\ \mathbf{b}_b \end{bmatrix} + \mathbf{F}(p_{\mathbf{i}}) = \Delta t\, \mathbf{D}^0 \begin{bmatrix} \mathbf{a}_b^* \\ \mathbf{b}_b^* \end{bmatrix} + \frac{4}{3} \pi {R_b}^3 (\rho_b - \rho)\, \mathbf{g}, \tag{42}$$

together with the remaining boundary conditions at physical boundaries of the fluid domain. Here $\mathbf{r}_{\mathbf{i}}^0$ and $\mathbf{x}_b^0$ are the initial locations of the interface and rigid body, and $\mathbf{a}_b^*$ and $\mathbf{b}_b^*$ denote initial guesses for the accelerations of the body. These latter quantities are taken to be

$$\mathbf{a}_b^* = \left(\frac{\rho_b - \rho}{\rho_b + 0.5\, \rho} \right) \mathbf{g}, \qquad \mathbf{b}_b^* = \mathbf{0},$$

which are the exact initial accelerations of a spherical particle in a viscous quiescent fluid of infinite extent. The computed added-damping tensor, denoted by $\mathbf{D}^0$, is included in (42) even though it is not required at $t = 0$ since added-damping effects are not instantaneous so that the discrete problem in (40)–(42) without $\mathbf{D}^0$ is well-posed. However, we have included the tensor intentionally to test the full linear system in a general case when $t > 0$. The corresponding discrete Poisson problem used in the TP-RB scheme involves the pressure equation in (40) with the interface condition

$$\mathbf{n}_{\mathbf{i}}^T \nabla_h p_{\mathbf{i}} = -\rho \mathbf{n}_{\mathbf{i}}^T \Big(\mathbf{a}_b^* + \mathbf{b}_b^* \times (\mathbf{r}_{\mathbf{i}}^0 - \mathbf{x}_b^0) \Big), \qquad \mathbf{i} \in \Gamma_h, \tag{43}$$

and the remaining physical boundary conditions. We note that the initial guesses for the accelerations in the interface condition for the TP-RB scheme is not as important since sub-iterations are needed at $t = 0$ to obtain a converged initial acceleration for this scheme.

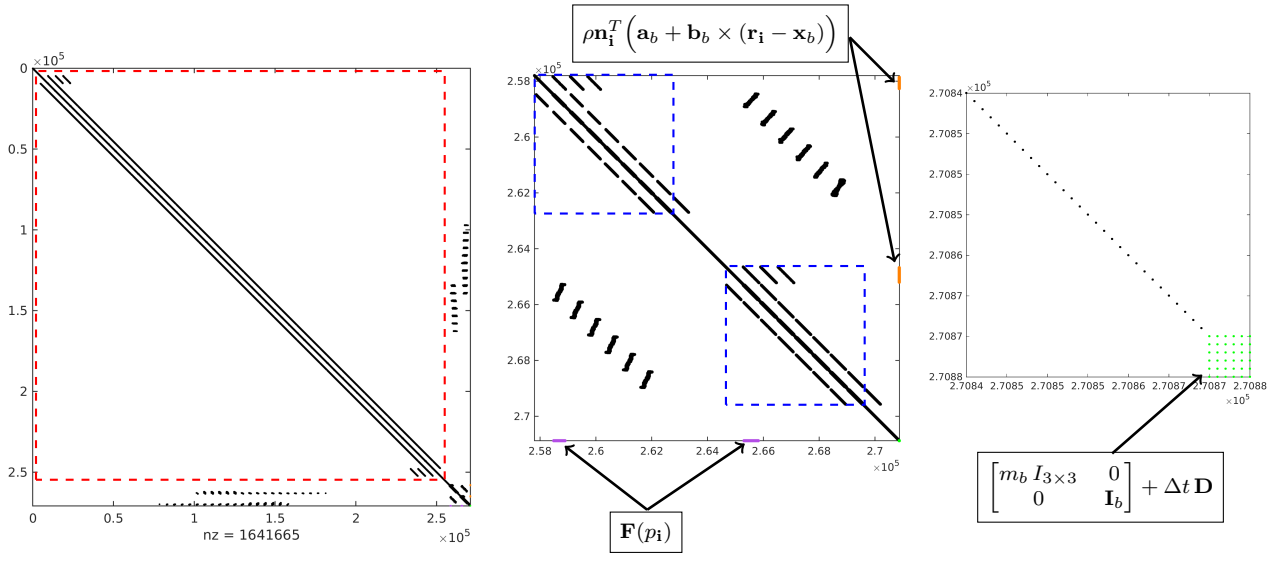

Figure 10: The sparsity pattern of the pressure matrix of 270875 × 270875 in the AMP-RB scheme. Left: the sparsity pattern from the grid $\mathcal{G}_{\text{sp}}^{(1)}$. Middle and right: two zoomed views of the pattern. The entries corresponding to the background Cartesian grid are marked by the red square and the entries of the two boundary fitted grids are marked by the blue squares. The important terms in the AMP interface conditions are marked in different colors and pointed out in the sparsity pattern.

Figure 10 shows the sparse matrix pattern of the linear system of the AMP-RB scheme for the grid $\mathcal{G}_{\text{sp}}^{(1)}$, which consists of one background grid and two boundary-fitted grids. The pressure matrix has a size

of 270875×270875 and can be divided into several blocks. The entries corresponding to the background Cartesian grid are marked by the red box in the figure, and the entries of the two boundary-fitted grids are marked by the blue boxes. The majority of the diagonal blocks correspond to the discrete Poisson operator, while the off-diagonal blocks correspond primarily to the interpolations between the different grids. The six AMP constraints in (42) related to the accelerations are positioned in the last rows of the matrix, and various terms in the constraints (41)–(42) have been marked by different colors and pointed out explicitly in the sparsity pattern. Apart from the six extra rows corresponding to the equations in (42) and the six extra columns for the accelerations of the body, the matrix of the new system is identical to that used in the TP-RB scheme.

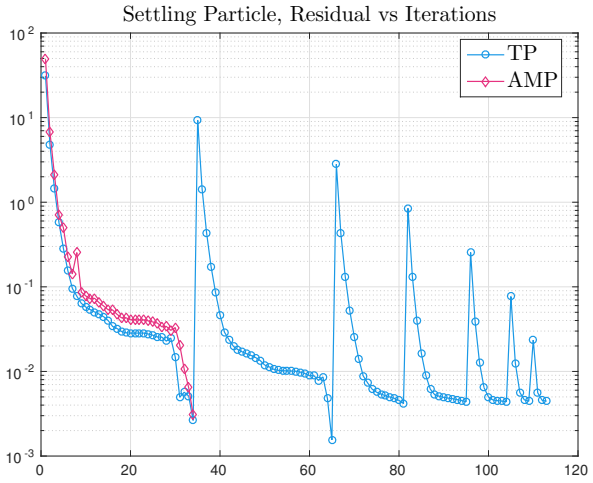

Pressure matrices of AMP-RB and TP schemes			
Scheme and Grid	$\sigma_{\max}$	$\sigma_{\min}$	Condition number
AMP on $\mathcal{G}_{\text{sp}}^{(1)}$	1.71	3.19e-5	5.34e4
TP on $\mathcal{G}_{\text{sp}}^{(1)}$	1.00	3.19e-5	3.13e4
AMP on $\mathcal{G}_{\text{sp}}^{(2)}$	1.49	8.04e-6	1.86e5
TP on $\mathcal{G}_{\text{sp}}^{(2)}$	1.01	8.02e-6	1.26e5

Figure 11: Left: residual verse iterations in the AMP-RB and TP schemes. Right: estimated condition numbers and other quantities of the pressure matrices in the two schemes. The sudden jump in the residual of the TP scheme on the left plot is due to the restart of the pressure solver in each sub-iteration. $\sigma_{\max}$ and $\sigma_{\min}$ are the estimated largest and smallest singular values. All the quantities in the right table are estimated through GMRES.

The linear systems for the two schemes are solved by a serial Bi-CGSTAB solver with an ILU(1) preconditioner. The Bi-CGSTAB solver is chosen because the matrix for a composite grid is typically not symmetric, and the Bi-CGSTAB solver often shows better performance than other Krylov solvers in this case. The ILU(1) preconditioner is chosen here because the system is relatively easily inverted and only a few Krylov iterations are needed to converge. Figure 11 presents the convergence of the residual for each sub-iteration. The AMP-RB scheme uses only one Krylov solve to obtain the solution, while the TP-RB scheme uses a Krylov solve for each of the seven sub-iterations needed for convergence of the whole system (corresponding to the sudden jumps of the residual in the figure). Note the performance of the Krylov iterations in the AMP-RB and TP-RB schemes is similar in the first solve, both using 33 Krylov iterations to obtain a convergent solution. This indicates the both systems are similarly conditioned. The subsequent sub-iterations for the TP-RB scheme require fewer and fewer Krylov iterations as the previous computed pressure serves as a better initial guess for the next sub-iteration.

To further understand the nature of the linear system, the condition numbers are estimated by the extremal singular values. The extremal singular values of the matrices are estimated by the singular values in the Hessenberg matrix of the GMRES iterations after about 1000 iterations. The table in Figure 11 shows that the largest singular value of the AMP-RB matrix is slightly larger than the TP-RB scheme while both schemes have almost identical smallest singular values which scale as $O(h^2)$. This confirms that the two systems have very similar conditioning. Recall that the condition number of the system is the ratio between the maximal and minimal singular values if the 2-norm is used. For the systems at a later time when $t > 0$, we find that the performance of the linear solver applied to the two systems is very similar to the case at $t = 0$, since the difference between the linear systems at two different times lies mainly in the right-hand side.

We further compare the total CPU time to solve the full problems given by the AMP-RB and TP-RB

Run-time performance of AMP versus TP												
Grid	rtol	atol	TP						AMP			
			rtolc	atolc	p/step	v/step	its/step	sec/step	p/step	v/step	sec/step	speed-up
$\mathcal{G}_{\rm sp}^{(1)}$	1e-5	1e-7	1e-4	1e-6	25	12	7	5.55	18	5	3.36	1.65
$\mathcal{G}_{\rm sp}^{(2)}$	2.5e-6	2.5e-8	2.5e-5	2.5e-7	53	16	8	40.8	39	6	23.6	1.73

Table 2: Settling particle. Comparison of the run-time performance of the AMP scheme versus the TP scheme. The relative and absolute tolerances of the velocity and pressure solvers are denoted by "rtol"and "atol", while the tolerances of the sub-iterations in the TP scheme are denoted by "rtolc" and "atolc". "P/step" and "v/step" stand for the averaged number of Krylov iteration in the pressure and velocity solvers per time-step, while "sec/step" for the averaged CPU run-time per time-step. The averaged number of iteration in the TP scheme are also given in the column of "its/step".

schemes. Table 2 presents detailed information of the two schemes on the grids $\mathcal{G}_{\rm sp}^{(1)}$ and $\mathcal{G}_{\rm sp}^{(2)}$. The grid $\mathcal{G}_{\rm sp}^{(1)}$ has about 2.2×10^5 total grid points, while $\mathcal{G}_{\rm sp}^{(2)}$ has about 1.7×10^6 points. Other information such as the tolerances in the Bi-CGSTAB solvers and sub-iterations in the TP-RB scheme are also provided in Table 2. The under-relaxation parameter in the TP-RB scheme (see [27]) is chosen to be 0.5, which we found to give the best performance for this problem. The results for $\mathcal{G}_{\rm sp}^{(1)}$ show that the CPU time of the AMP-RB scheme is about 3.36 seconds per time step, while the time of the TP-RB scheme is about 5.55 seconds per time step, which corresponds to a speed-up factor of 1.65 the AMP-RB scheme. Note the TP-RB scheme for this problem requires about 7 sub-iterations for each time step, but the performance of the AMP-RB scheme only has increased by a factor of 1.65. This is expected since, as demonstrated in Figure 11, the later correction steps in the TP-RB scheme require fewer Krylov iterations than first two steps. In a typical time step, the predictor and the first corrector in the TP-RB scheme account for most of the Krylov iterations in the pressure solver ("p/step" in Table 2) and the further correction steps only require one or two Krylov iterations to obtain a converged local solution. Note that for both schemes, each Krylov iteration takes almost the same CPU time on average, although the linear system for the AMP-RB scheme is slightly larger. The $\mathcal{G}_{\rm sp}^{(2)}$ results show a similar speed-up factor of 1.73. The CPU time of the AMP-RB scheme is about 23.6 seconds per time step for this grid, while the time of TP-RB scheme is about 40.8 seconds per time step. Note also that the tolerances of each sub-iteration in the TP-RB scheme are chosen larger than the tolerances of the Krylov solver to avoid too many sub-iterations. We have found that this choice is sufficient to yield satisfactory numerical solutions. However, if the tolerances for the sub-iterations and Krylov solvers are chosen to be the same, the AMP-RB scheme is about 4 times faster than the TP-RB scheme. Finally, note that the current overhead in various other parts of the schemes, such as computing information related to the overlapping grids and evaluating the advection terms, are roughly the same in both schemes. For instance, the overhead accounts for about 15% of the "sec/step" in the AMP-RB scheme and it accounts for about 10% for the TP-RB scheme.

In summary, the above tests show the new linear system in the AMP-RB scheme to solve the discrete Poisson problem for the pressure requires only minor modifications to the corresponding linear system for pressure in the TP-RB scheme. Both systems have similar conditioning and can be solved effectively using preconditioned iterative Krylov solvers. The AMP-RB scheme requires no sub-iterations per time step unlike the TP-RB scheme so the cost per time step for the AMP-RB scheme is lower. As the ratio of the density of the rigid body to that the fluid becomes smaller, the TB-RB scheme requires more and more sub-iterations (and ultimately fails). In contrast, the AMP-RB scheme does not require sub-iterations and so the comparative performance of the AMP-RB scheme is more pronounced for lighter bodies, such as in the problem discussed in the next section.

5.4. One particle falling or rising in a long container

The next validation problem we consider is a spherical particle falling or rising due to a buoyant force in a very long container. The original problem was discussed in an experimental study [55], but then used later in [12] to validate an immersed boundary method. In many subsequent studies of FSI algorithms, such as those in [17, 20, 30, 56], Case 2 in [12] has been adopted as a standard benchmark problem to demonstrate numerical stability for problems involving low-density particles. The problem shares a very similar geometry

as the particle dropping test discussed in the previous two sections, but the size of the particle here is much smaller compared to the computational domain. We follow the nondimensional setup from the work in [12, 17]. An incompressible fluid with viscosity $\mu = 0.00104238$ and density $\rho = 1$ occupies the domain $[-x_c, x_c] \times [-y_c, y_c] \times [z_0, z_1]$, where $x_c = y_c = 0.64$, $z_0 = 0$ and $z_1 = 10$. The particle has a density of ρ_b and a radius of $R_b = 1/12$. The fluid and the particle are initially quiescent and an impulsive external body force satisfying (38) with $\tilde{g} = 9.81$ is applied at $t = 0$. In [12] the particle was initially located at $\mathbf{x}_0 = (0, 0, 9.5)$ and the density of particle is $\rho_b = 2.56$. However, in more recent work the particle density has varied, and the velocity profile of the particle for different values of ρ_b are presented. In our simulations, the particle is initially located at $\mathbf{x}_0$ for cases when the particle falls ($\rho_b > 1$), and it is located at $(0, 0, 0.5)$ initially for cases when it rises ($\rho_b < 1$). Periodic boundary conditions are applied in all three directions as in the previous work [12, 17].

The original problem is designed to model the situation when the particle is immersed in an infinite fluid domain. The composite grid approach allows us to use a coarser background grid than the previous work [12, 17] and at the same time attach much finer boundary-fitted grids to the particle so that its boundary layer and the particle wake are well resolved. The sphere-in-a-box composite grid similar to the previous case is used with slight modifications. A target mesh spacing $h = 0.02$ is used for the background Cartesian grid, corresponding to a grid of $64 \times 64 \times 500$ covering the entire domain. Much finer boundary-fitted grids are attached to the particle and cover the fluid region of length $\Delta r = 0.3$ in the radial (normal) direction. The target mesh spacing for the boundary-fitted grids is $h/4 = 0.005$. Here we use a three-patch sphere to avoid excessively small time steps resulting from small cells in the two-patch version. The resulting composite grid[6], consisting of the background grid and three boundary-fitted grids, is denoted by $\mathcal{G}_{\text{sr}}$. A fixed time step, $\Delta t = 0.001$, is used in all the simulations.

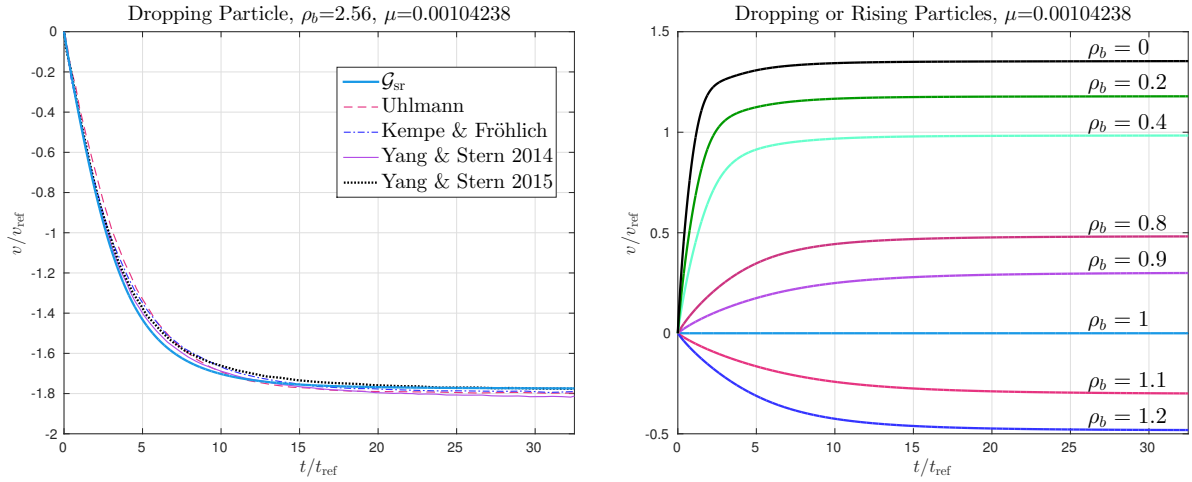

Figure 12: Dropping or rising particle. Time history of the velocity (left) of the case $\rho_b = 2.56$ and velocity (right) of the varying density cases. The reference velocity and time are $v_{\text{ref}} = \sqrt{2R_b\tilde{g}}$ and $t_{\text{ref}} = \sqrt{2R_b/\tilde{g}}$, where $R_b = 1/12$ and $\tilde{g} = 9.81$. The solutions are computed on grid $\mathcal{G}_{\text{rs}}$. In the left plot, the red dashed curve is the numerical solutions taken from Fig. 16 in [12], the blue dash-dotted curve is from Fig. 11 in [17], the purple curve is from Fig. 5 in [56] and the black dotted curve is from Fig. 10 in [20].

The left plot in Figure 12 shows the time history of the particle velocity for the case $\rho_b = 2.56$. The numerical solution given by the AMP-RB scheme is compared with the results found in the literature [12, 17, 20, 56] using different immersed boundary methods. Our results are in good overall agreement with these results. The computed terminal speed is found to be $v_{\text{term}} = 1.774\, v_{\text{ref}}$, which is in good agreement with the experimental terminal speed of 1.797 reported in [55]. We observe that the particle drops slightly faster at early times in our simulation as compared to the results from the immersed boundary methods, although all of the simulations produce similar terminal speeds. We also observe that the particle wake does not break

[6]The interested reader is again referred to [38] for more details on the sphere-in-a-box grid.

in our simulations and remains axisymmetric, even when a finer grid is used. Whether the particle wave remains axisymmetric or not can effect the profile of the particle velocity, and this differs in the various simulations. For example, the numerical results in [12] show an asymmetric wake, which triggers much larger horizontal velocities than what we observe, while the wake remains axisymmetric for the simulations discussed in [56]. Whether the wake remains axisymmetric or not is likely due to a hydrodynamic instability and whether this instability is triggered by perturbations in the flow due to the treatment of the moving grids in the vicinity of the particle. We observe, for example, that a similar simulation using the TP-RB scheme (with sub-time-step iterations) with the same composite grid $\mathcal{G}_{\text{sr}}$ shows an axisymmetric wake and a nearly identical velocity profile to that given by the AMP-RB scheme. This suggests that the issue is not related to the treatment of the interface conditions in the AMP-RB scheme.

The results from varying density tests are also presented in Figure 12, where the time history of velocities of selected particle densities are presented. The AMP-RB scheme remains stable for any density ratio, including the case $\rho_b = 0$, while the previous methods appear to be unable to compute solutions for low density ratios. For example, to our knowledge, the lowest stability bound of this particular benchmark test was previously presented in [20], in which their scheme is stable for $\rho_b/\rho \geq 0.1$. On the other hand, the TP-RB scheme in our implementation also struggles to remain stable for small density ratios. For instance, when $\rho_b/\rho = 0.1$, the TP-RB scheme needs about 9 sub-iterations to converge on average. When the body density is 0.01, the TP-RB scheme struggles and needs about 85 sub-iterations to converge on average, which makes the scheme significantly more expensive. It is difficult to stabilize the TP-RB scheme for even small density ratios.

5.5. Numerical simulations of a mechanical heart valve

The last example we consider is a model of a bi-leaflet mechanical heart valve, which has been studied previously in [15, 35], for example, using other numerical approaches. As shown in Figure 13, the heart valve consists of a rigid cylindrical ring supporting two solid leaflets, which can rotate about fixed hinge axes. The heart valve is placed in a fluid channel which models the aorta. The structure of each leaflet is designed to be very thin so that its inertia is small compared to that of the fluid flowing through the device. Previous studies have found this system to be very challenging to simulate mainly due to large added-mass effects [15]. Therefore, this problem serves as a good test to demonstrate the applicability of the AMP-RB scheme together with the moving composite grid approach for a challenging engineering problem of significant interest. The problem also can be used as a good benchmark problem for other FSI algorithms. Unfortunately, a well-specified benchmark problem based on this application is not currently available in the literature to the best of our knowledge. The results of previous simulations are available, but the input to these simulations is based on experimental data, and there is incomplete information given on the initial conditions or boundary conditions in many cases, so that it is difficult to reproduce the results for the purpose of quantitative comparisons. Thus, another focus of the present study is to fully specify benchmark problems based on the bi-leaflet geometry for both two and three-dimensional FSI simulations. From the point of view of FSI algorithms and added-mass effects, the difficult interval of the full cardiac cycle involves the rapid rotation of the leaflets as the value opens and closes. Hence, the designed benchmark problems and our simulations focus on this aspect of the application.

As illustrated in Figure 13, the fluid channel covers a cylindrical domain with length $L_c = 1.75$ and radius $R_c = 1.1$. The left boundary is located at $x_0 = -0.5$ and the right boundary is $x_1 = 1.25$. The valve is fully immersed in an incompressible fluid with density $\rho = 1$ and viscosity $\nu = 0.1$. Two leaflets are allowed to rotate along the hinge axes, which are located at $(x_b, y_b) = (0, \pm 0.15)$ and parallel to z-axis, and the leaflets are attached to the hinge at the position 0.1 away from the bottom tips. The range of angles for the leaflets are $[\theta_{\min}, \theta_{\max}]$ with $\theta_{\min} = 10^\circ$ and $\theta_{\max} = 75^\circ$, which corresponds to the fully open and closed heart valve. While the precise shape of the leaflets are given later for the specific cases of two and three-dimensional flow, they are assumed to have the same moment of inertia given by $I_b = 0.001$ as used in [15]. The leaflets are considered to be "light" as added-mass effects corresponding to their rotational motion are large for this test.

During the operation of the actual mechanical heart valve, the limits of the rotation angles of the leaflets are reached at points of solid-solid contact. In our numerical simulations, such contacts are avoided by imposing the tighter limits on the rotation angles as given above. These chosen limits could be imposed in the numerical solution using a post-processing step immediately following any time step for which the

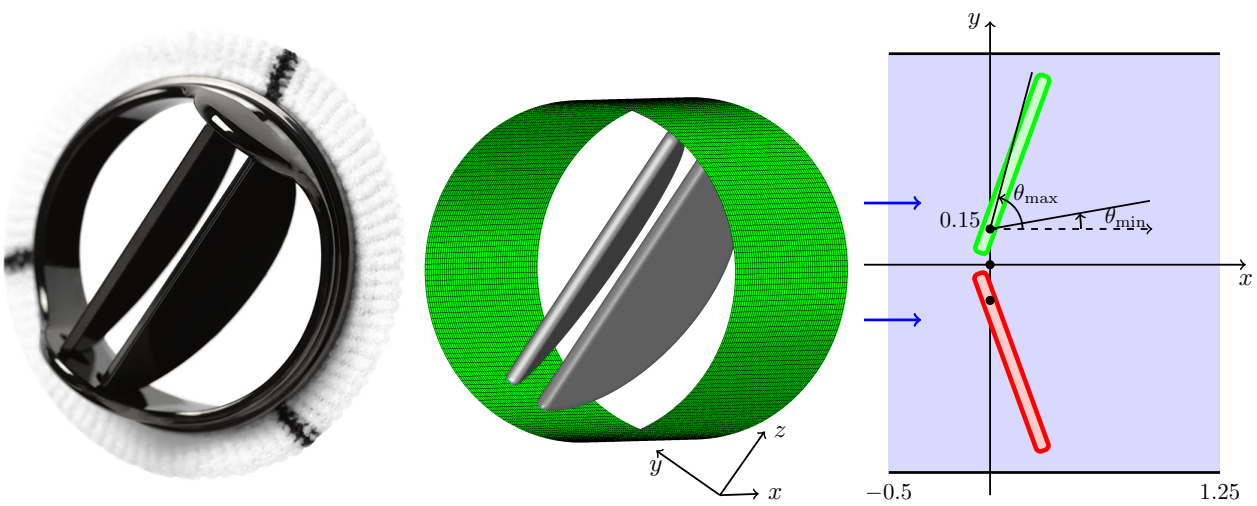

Figure 13: Mechanical heart valve. Left: a typical bi-leaflet mechanical heat valve (SJM Regent). Middle: leaflets and the computational domain. Right: geometrical configuration at the symmetry plane of the domain ($t = 0$).

rotation limits have been exceeded. While this approach appears to be a simple choice to implement, we have found that the resulting abrupt perturbation to the solution can lead to numerical instabilities. Thus, we have adopted an alternate approach in which a continuous repulsive force is applied to the equations of motion of the leaflets to smoothly restrict their rotation to the chosen range. In addition, we apply a damping term to the equations of motion to model the loss of energy that would occur during a collision. The equation of motion for the angular acceleration of each leaflet is thus taken to be

$$I_b\,\dot{\omega}_b = \int_{\Gamma_b} \mathbf{e}_z^T \Big[(\mathbf{r} - \mathbf{x}_b) \times \boldsymbol{\sigma}\mathbf{n}\Big]\, dS + g_{\rm rt}(\theta_b) - B(\theta_b)\,\omega_b, \tag{44}$$

where $g_{\rm rt}(\theta_b)$ is the repulsive torque and $B(\theta_b)\,\omega_b$ is the damping term. Formulas for the functions, $g_{\rm rt}(\theta_b)$ and $B(\theta_b)$, are given in (A.9) and (A.10), respectively, of Appendix A where a full description of the contact model is given. Here, we note that these terms are set to zero except for a small angle δ near the limits of the range of rotation. This angle in (A.9) and (A.10) is taken to be $\delta = 3°$ for all of our simulations. The stiffness parameters in (A.9) are taken to be $\epsilon_1 = 0.05$ and $\epsilon_2 = 0.01$, for the open and closed states, respectively, and the damping parameter in (A.10) is $B_0 = 20$. The stiffness parameter near the closed state, ϵ_2, is chosen to be smaller than that near the open state, ϵ_1, because the collision between the leaflets and hinges is more violent as the valve closes. The parameters given above specify our collision model, and they are fixed for all of our choices of the grid resolution in our FSI simulations of this problem.

The fluid flow through the heart valve is driven by a pressure difference between the left and right boundaries, which models the changing of blood pressure in a cardiac cycle. On the left boundary, $x_0 = -0.5$, the transverse velocity is set to be zero, while the pressure is taken to be

$$p(x_0, y, z, t) = \begin{cases} p_{\max}\,\sin(\pi t) & \text{if } 0 \le t \le 1, \\ p_{\min}\,\sin(2\pi t) & \text{if } 1 < t \le 1.25, \\ p_{\min} & \text{if } t > 1.25, \end{cases} \tag{45}$$

with $p_{\max} = 20$ and $p_{\min} = -40$. The magnitude of the minimum pressure $p_{\min}$ is chosen to be larger than the maximum pressure $p_{\max}$ to mimic a typical cardiac cycle, in which the magnitude of the difference between ventricular and aortic pressure is larger in diastole than systole. The boundary condition at $x_1 = 1.25$ is a zero-pressure outflow/inflow condition, which is implemented by setting

$$p(x_1, y, z, t) = 0, \qquad \frac{\partial \mathbf{v}}{\partial n}(x_1, y, z, t) = \mathbf{0}.$$

This boundary condition allows the fluid to flow from left to right during the opening process, and then flow backwards during the closing process. The remaining boundary conditions on the surface of the leaflets and

on the walls of the cylinder are taken as no-slip walls. The fluid is at rest initially and the leaflets are also at rest in a closed state at the rotation angles $\pm 70^\circ$. The time step is determined using a CFL number of 0.9, which is based on the advection terms in the fluid momentum equations.

The AMP-RB sheme used here avoids sub-time-step-iterations between the fluid and solid equations by handling added-mass and added-damping effects in the AMP interface conditions, whereas the previous work for this problem employed various TP-RB schemes [15, 35]. Some discussion of added-mass effects for this heart-valve problem can be found in [15]. In this paper, both a loosely-coupled FSI algorithm (i.e., a TP-RB scheme without sub-iterations) and the strongly-coupled FSI algorithm (i.e., a TP-RB scheme with sub-iterations) are considered. It was concluded that the TP-RB scheme without sub-iterations is unstable regardless of the size of the time step for the problems involving bodies of small inertia, and the TP-RB scheme with under-relaxed sub-iterations and the Aitken's acceleration technique is required for certain difficult problems with strong added-mass effects. Our finding for this problem, and the theoretical results in our previous work [1], are consistent with the results described in [15].

To better isolate the different issues and to clearly illustrate the results, we first consider simulations of the heart-value problem in two dimensions. This reduction can be viewed as an approximation of the flow along the symmetry plane of the three-dimensional domain. We note that the two-dimensional problem shares many of the important numerical difficulties as the full three-dimensional problem, such as strong added-mass effects, and this problem is reasonable as a starting point and forms a good benchmark problem. We then conclude our numerical investigations with simulations of the heart-valve problem in three dimensions. The three-dimensional benchmark problem is closer to a realistic geometry in which two half-disk leaflets are used to model the heart valve.

5.5.1. Benchmark problem in two dimensions

For the two-dimensional version of the heart-valve problem, we consider a fluid channel with horizontal and vertical extent corresponding to the symmetry plane of the three-dimensional domain described previously. This implies a channel covering the domain $[x_0, x_1] \times [-R_c, R_c]$ with $x_0 = -0.5$, $x_1 = 1.25$ and $R_c = 1.1$. Here, each leaflet is a rectangle (with rounded corners) of length and width equal to 1.0 and 0.1, respectively. The composite grid for the domain, denoted by $\mathcal{G}_{\rm ts}^{(j)}$, consists of one background Cartesian grid and two boundary-fitted grids as shown in Figure 14. The background grid has a grid spacing given by $h_j = 1/(40j)$, where j is a refinement factor. The boundary-fitted grids are stretched in the normal direction to the surface of the leaflets. The resulting grid spacing is close to h_j for the grid lines away from the surface and overlapping with the background grid, while the grid spacing in the normal direction is reduced by a factor of approximately 4 near the surface. The equation of motion in (44) for each leaflet reduces to

$$I_b\,\dot{\omega}_b = \int_{\Gamma_b} \left(\tilde{\mathbf{r}}^T \boldsymbol{\sigma}\mathbf{n}\right) ds + g_{\rm rt}(\theta_b) - B(\theta_b)\,\omega_b, \tag{46}$$

where $\tilde{\mathbf{r}} = (-r_2 + y_b, r_1 - x_b)^T$ for the line integral around the body Γ_b in (46). The center of mass of the two leaflets given by $(x_b, y_b) = (0, \pm 0.15)$ initially is nearly fixed during the simulations due to very large value for m_b taken in (5).

The instantaneous streamlines of the numerical solution at selected times are presented in Figure 15, and the corresponding rotation angle, angular velocity and acceleration of the upper leaflet are given in Figure 16. (The latter figure also indicates grid convergence which is discussed below.) At early times, the pressure at the left boundary increases according to the prescibed profile in (45), and this drives the fluid to the left causing the leaflets to open (see the streamline plots at $t = 0.2$ and $t = 0.5$). At approximately $t = 0.6$, the leaflets approach the lower limit of the rotation angle given by $\pm\theta_{\rm min}$, and they exhibit a small oscillation due to combined influences of the fluid, repulsive force and damping term as shown in the time history of the leaflet motion in Figure 16. By about $t = 0.8$, the fluid force on the leaflets balances the repulsive force, and hence the leaflets appear to reach a steady state. Through this time, starting at $t = 0.5$, the applied pressure on the fluid at the left boundary has been decreasing, and after $t = 1$ the pressure is negative. The effect of this negative pressure is first seen in the plot of the instantaneous streamlines at $t = 1.1$, where a relatively small region of reverse flow is observed at the right-hand side of the channel near the centerline, $y = 0$. By $t = 1.2$, the flow is in the midst of reversal and several vortices have formed in the channel as a result. Meanwhile, the leaflets have started to swing back towards their closed position as a

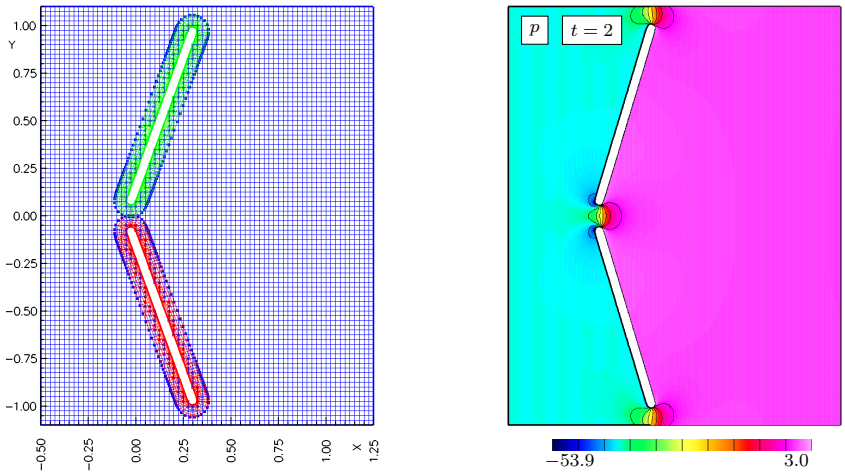

Figure 14: Mechanical heart valve in 2D. Left: Composite grid $\mathcal{G}_{\rm ts}^{(1)}$ at $t = 0$ (coarse grid). Right: contours of the pressure at $t = 2$ using grid $\mathcal{G}_{\rm ts}^{(8)}$.

result of the reversed flow. The leaflets approach their closed position at approximately $t = 1.6$, and again an oscillation in the rotation angle about the limit state is observed. This motion is similar to that during the opening stage, but the oscillation is more severe since the leaflets close faster due to a larger magnitude of the pressure difference in the prescribed pressure profile during the closing process. After $t = 1.6$ the oscillations are significantly reduced by the damping term, and the leaflets reach another steady state corresponding to a closed valve.

The time history of the behavior of the top leaflet, presented in Figure 16, is used to illustrate the grid convergence of solutions of the AMP-RB scheme for this problem. In each plot, four curves are shown corresponding to the time history of the rotation angle, angular velocity and acceleration from calculations using composite grids of increasing resolution. We note that the separation between curves decreases rapidly as the grid resolution increases. However, the zoomed view in Figure 16 of the acceleration at later times of the simulation, shows that the convergence of this component of the solution is not as clean. To give a quantitative sense of the convergence rate, Richardson extrapolation is used to estimate the time-averaged convergence rate of the three finest grids. At an early time, $t = 0.5$, the estimated convergence rates of the rotation angle, angular velocity and acceleration are 1.51, 1.40 and 1.44, respectively. The rates drop to 1.36, 1.32 and 1.24 at $t = 1$, and then to 1.19, 1.15 and 0.89 at the final time $t = 2$. The reduced convergence rates at later times are largely due to the collision model. For instance, the convergence of the acceleration is poor during the closing stage, as noted earlier and shown in the zoomed view of the acceleration. Generally, we find that the grid convergence is sensitive to the choices of the parameters in the collision model, such as ϵ and B_0. Realistic simulations require a stiff collision model, so that very fine grids with correspondingly small time steps would be needed to get better convergence results, especially during the closing stage of the simulation.

We note that because our FSI model simulation has avoided solid-solid contacts, the channel is not complete blocked by the two leaflets in their closed position. The result of this choice is that there is some small leakage of the fluid between the two leaflets and between the leaflets and the walls of the channel when the valve is in its closed position. We also note that the Reynolds number of flow for the current simulation is $\mathrm{Re} = U_{\max} D/\nu \approx 100$, where $D = 2R_c$ is the channel width and $U_{\max}$ is the peak speed of the flow at the inlet. The Reynolds number for the simulations in [15, 35] was reported to be larger, approximately 6000 or more. We have chosen to compute the flow in the heart value using a larger viscosity, and thus a smaller Reynolds number, so that sufficient grid resolution of the flow can be achieved, especially for the subsequent benchmark calculations in three dimensions. Finally, we note that our version of the TP-RB scheme is not able to compute solutions for this problem since we are not able to find a fixed value for the relaxation parameter to stabilize the scheme through the under-relaxed iterations. As suggested in [15], Aiken's convergence acceleration may be necessary to stabilize the TP-RB scheme for this case. In contrast,

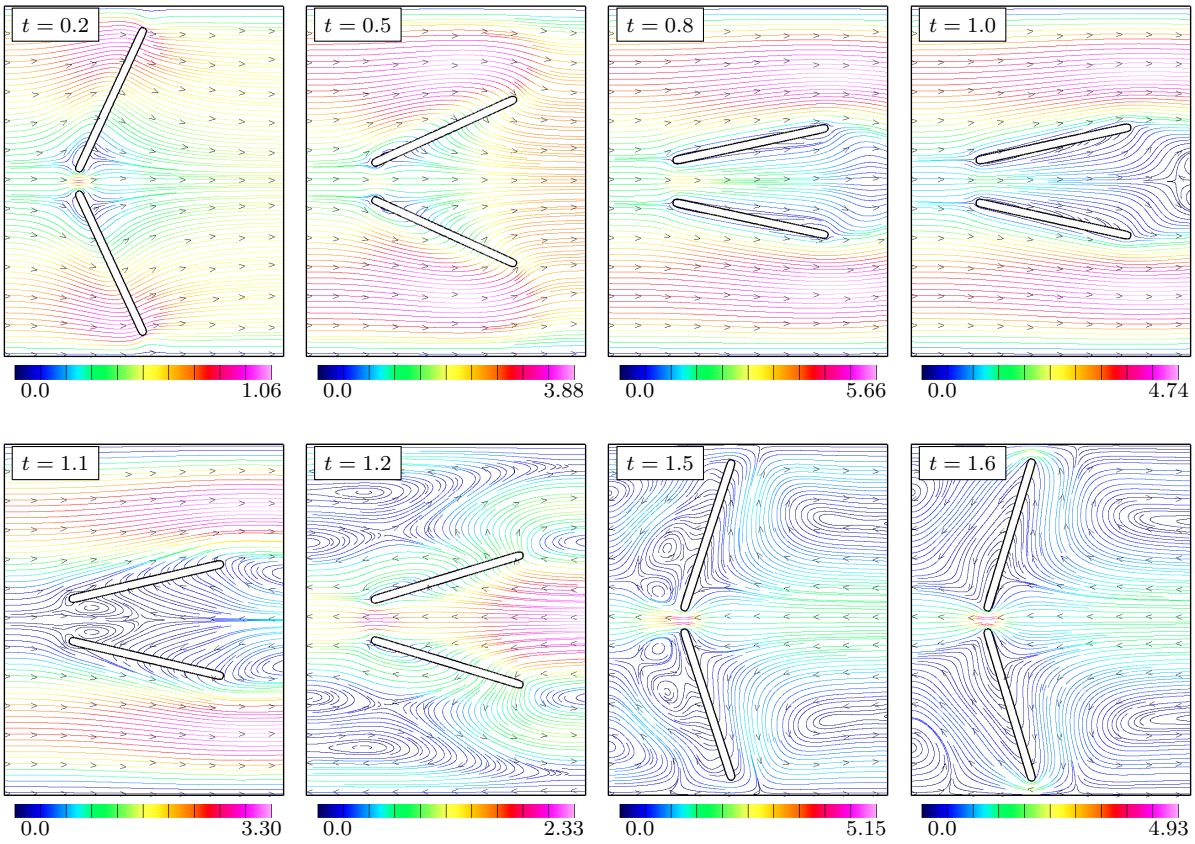

Figure 15: Mechanical heart valve in 2D. Computed instantaneous streamlines (colored by the flow speed) at selected times using the composite grid $\mathcal{G}_{\rm ts}^{(8)}$.

the AMP-RB scheme remains stable throughout the whole simulations.

5.5.2. Benchmark problem in three dimensions

The geometry of the two leaflets and their position in the cylindrical channel for the three-dimensional heart-value problem are illustrated in Figure 17. A thin disk of width $L_\ell = 0.1$ and radius $R_\ell = 1$ is split into two halves to obtain two leaflets. To allow the leaflets to rotate without colliding into each other, a thin portion of the half-disk along its equator is removed so that the height of the resulting solid is 0.95, which is shorter than its radius R_ℓ. The edges of the two leaflets are rounded to avoid sharp corners (similar to that done in the two-dimensional problem). The above process to define the geometry is done using a computer-aided design (CAD) program. Figure 17 also shows the surface grids on the leaflets and the composite grid. The composite grid, denoted by $\mathcal{G}_{\rm hv}^{(j)}$ with resolution factor j, consists of two background grids and the collection of boundary-fitted grids that represent the leaflets as shown in the figure. The first background grid is a Cartesian grid, with target grid spacing $h_j = 1/(40j)$, covering the bulk of the fluid channel, while the second grid is a thin boundary-fitted grid, with grid spacing $2h_j/3$, attached to the cylindrical boundary of the channel. (The Cartesian grid is not shown in the figure so that the position of the leaflets can be seen, and only the boundary of the cylindrical boundary-fitted grid is shown.) The surface of each leaflet is divided into three grids, two surface grids of grid spacing h_j on the two faces of the half-disks and one edge grid of grid spacing $2h_j/3$ forming the perimeter of the solid. The two surface grids and the edge grid are then extended to the volume, with target grid spacing $2h_j/3$, to form the three-dimensional boundary-fitted grids around the leaflet. The composite grid is generated using the **Ogen** grid generator. The IGES file generated by the CAD program provides the input to form the surface and edge grids for the leaflets, and then Ogen generates the body-fitted volume grids and creates the composite grid from these

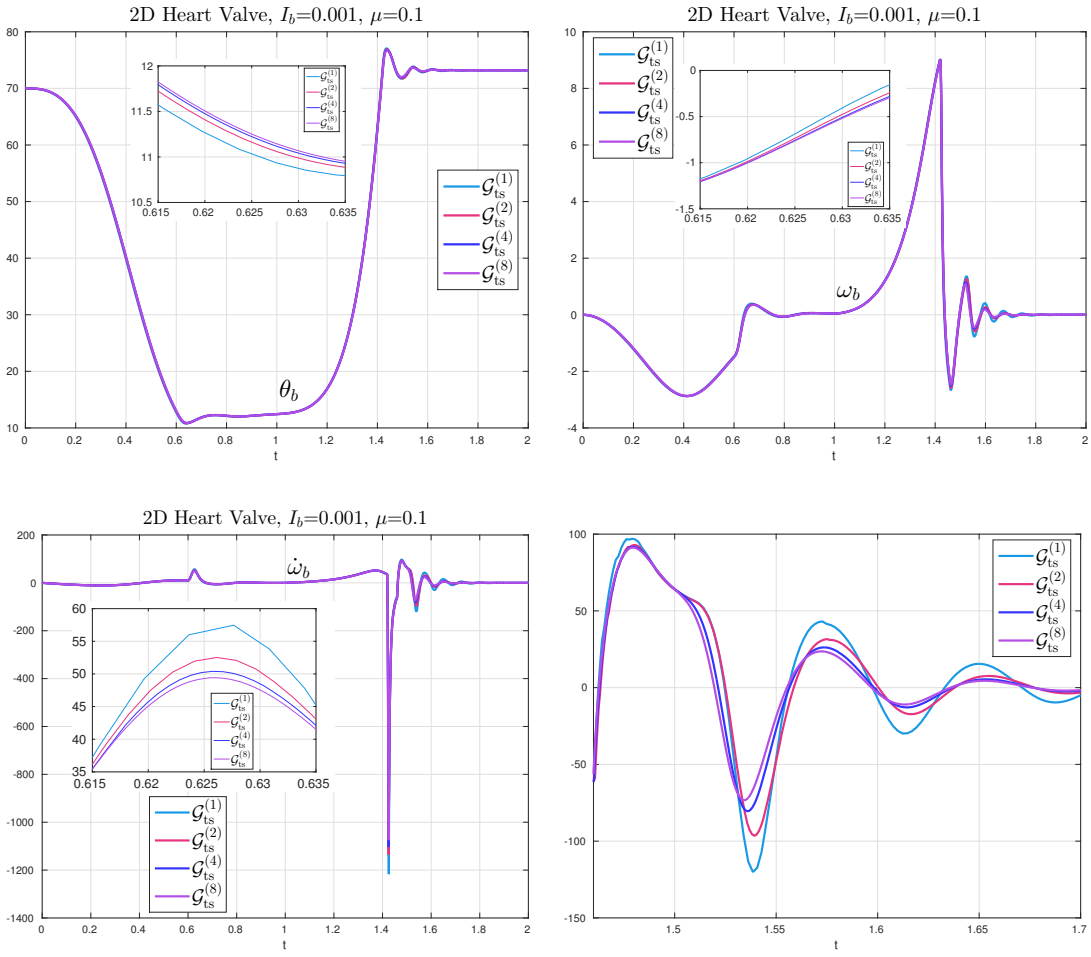

Figure 16: Mechanical heart valve in 2D. Time history of the rotation angle (top left), angular velocity (top right) and acceleration (bottom left) of the top leaflet. Several zoomed views are presented including the zoomed view of the accelerations at the later time (bottom right). Results are shown from calculations using the composite grid, $\mathcal{G}_{\rm ts}^{(j)}$, $j = 1, 2, 4, 8$.

grids along with the two background grids as described above. For more details on generating grids from a CAD geometry, see [57].

The behaviour of the numerical solution at selected times during the simulation of the three-dimensional heart-value problem is shown in Figure 18. Colour contours of the fluid pressure on the surface of the leaflets is shown along with the instantaneous streamlines from a collection of tracer particles which illustrate the flow around the leaflets. The images along the top row of the figure at times $t = 0.2$, 0.4 and 0.6 are chosen to illustrate the behaviour of the solution as the valve opens. The starting points for the tracer particles in these images lie on the plane $x = x_0 = -0.5$ at the left boundary of the fluid channel, and are positioned in the shape of a cross. There are seven tracers along the vertical line segment of the cross with $x = -0.5$ and $z = 0$, and there are four tracers along its horizontal line segment with $x = -0.5$ and $y = 0.5$. At the earliest time, $t = 0.2$, we observe that the instantaneous streamlines from some of the tracers stagnate on the surface of the leaflets indicating that the flow is blocked, while at later times the streamlines from these tracers show that the flow passes over and around the leaflets as the valve opens. The bottom row of images in Figure 18 at the times $t = 1.2$, 1.4 and 2.0 are shown to illustrate the flow while the valve closes. For these images, the starting points of the tracers are positions on the plane $x = 1.1$ near the right boundary of the channel. Seven tracers are located along the verticle line with $x = 1.1$ and $z = 0$, while four more tracers are located along the horizontal line with $x = 1.1$ and $y = 0.5$, all forming a cross shape similar to before. At $t = 1.2$, we note a recirculation zone near the tip of the top leaflet as the flow reverses due to a

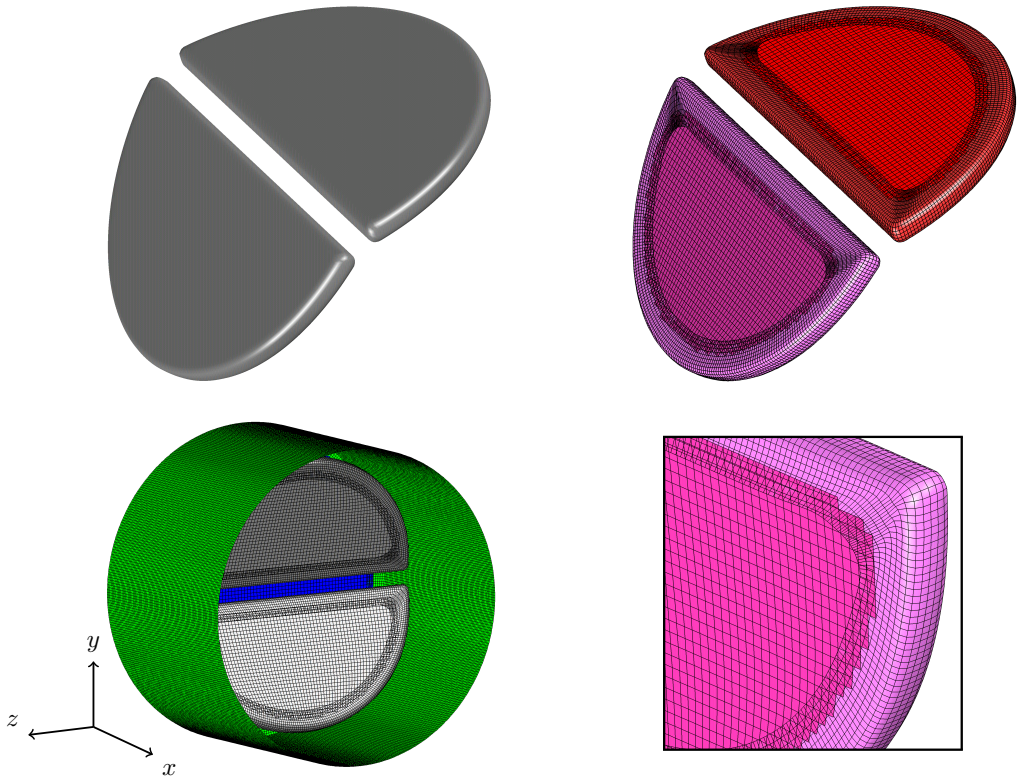

Figure 17: Mechanical heart valve grid in 3D. Top left: the CAD geometry represented as the surface of two leaflets. Top right: surface grids generated with the hyperbolic grid generator. Different surface grids have been colored by different colors. Bottom left: the composite grid at $t = 0$. Bottom right: zoomed view of the corner of the bottom leaflet. The presented grids are from $\mathcal{G}_{\text{hv}}^{(1)}$ (coarse grid).

change in the sign of the prescribed pressure profile in (45). At the two later times, the flow again becomes blocked as the valve closes, but with some leakage as noted earlier. However, there is a significant region of near stagnant flow on the face of leaflet as indicated by the near uniform pressure there.

The time history of the motion of the top leaflet is presented in Figure 19. Overall, the motion of leaflet is similar to that observed in the two-dimensional case, and shown previously in Figure 16. For example, there is a slight oscillation seen as the leaflet approaches its lower limit, θ_{min}, at the open position. There is a brief interval of time where the leaflet is in equilibrium at its open position, prior to a rapid rotation of the leaflet towards the upper limit, θ_{max}, at the closed positon. Near the upper limit there is a stronger oscillation, also observed in the two-dimensional case, as the stress on the leaflet from the fluid achieves a balance with the stiff repulsive force of the contact model. The oscillation dampens in time due to the damping term in the model, and an equilibrium is again reached but now with the valve in the closed position. In Figure 19 for the three-dimensional case, there are three curves drawn in each plot corresponding to the results computed using the composite grid, $\mathcal{G}_{\text{hv}}^{(j)}$, with increasing values of the resolution factor $j = 1$, 2 and 4. This is done to indicate the grid convergence of the solutions. In the plots of the rotation angle θ_b, the angular velocity ω_b and the acceleration $\dot{\omega}_b$, we see that the curves from the solutions on the different grids lie nearly on top of one another, as was seen for the two-dimensional benchmark problem. The differences in the curves can be seen in the zoomed views, and in these views we observe a convergence in the behaviours as the grid is refined. Estimates of the convergence rate for the angular velocity and acceleration are 0.92 and 1.46, respectively, while the convergence rate for the rotation angle is 0.30. The convergence rates found in the three-dimensional case are generally lower than the ones found in the two-dimensional case for this difficult problem. This is likely due to the coarser grids used to compute the convergence estimates for the three-dimensional case.

As in the two-dimensional benchmark problem, we are not able to find a stable under-relaxed parameter

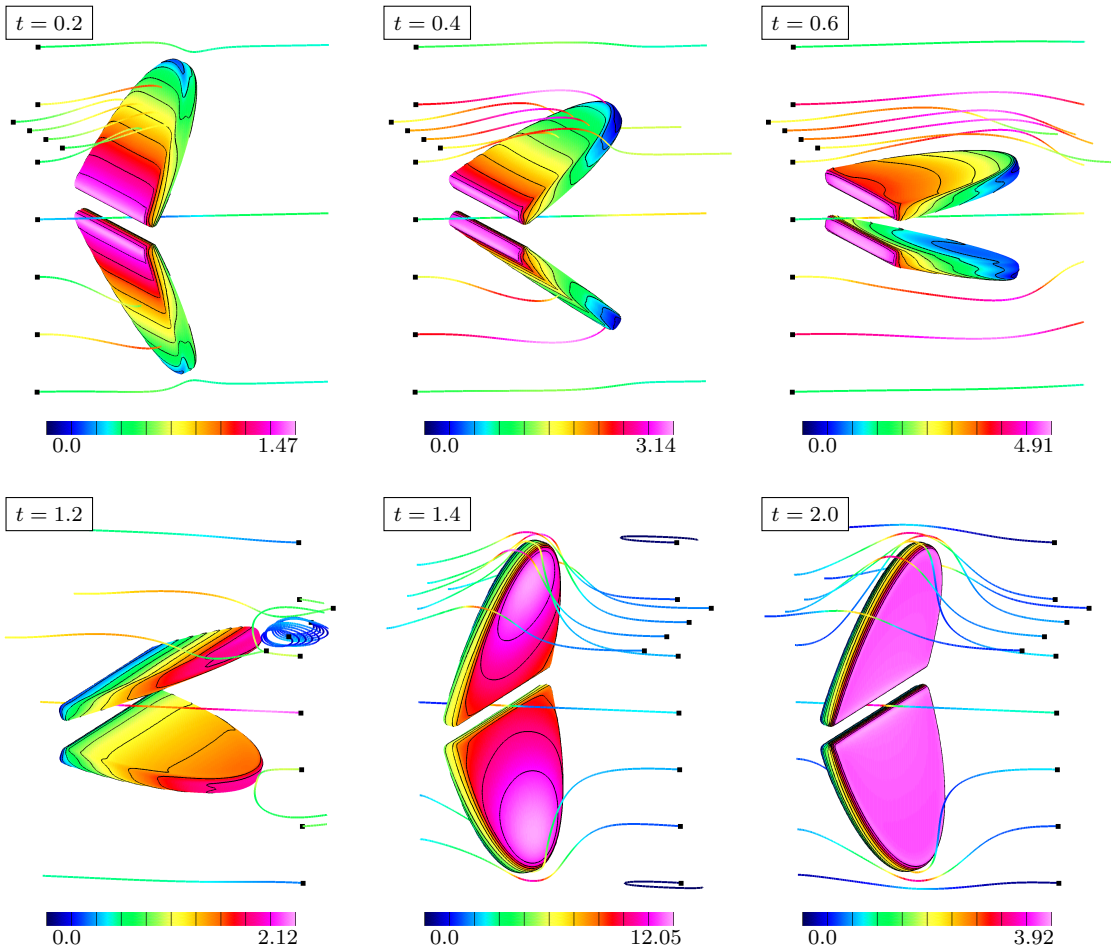

Figure 18: Mechanical heart valve in 3D. Computed instantaneous streamlines (colored by the flow speed) at selected times using the composite grid $\mathcal{G}_{\text{hv}}^{(2)}$. The colorbars are provided for the flow speed. The pressure is plotted on surface of the leaflets.

for our version of the TP-RB scheme when simulating the problem in three dimensions. The TP-RB scheme typically becomes unstable after a couple of time steps even with under-relaxed sub-iterations. In contrast, the AMP-RB scheme remains stable throughout the whole simulation.

6. Conclusion

In this work we have extended the AMP-RB scheme derived in [1, 2] to three dimensions for FSI problems with rigid bodies moving in an incompressible fluid. The extension relies on the moving overlapping grid approach, parallel implementation based on MPI and various building blocks handled properly in three dimensions. Several details of the full three-dimensional algorithm have been described, including the AMP interface condition handling the added-mass and added-damping effects, a strategy to find the surface quadrature on composite grids, and parallel implementation such as parallel partitioning and sparse linear solvers. This work confirms the AMP-RB scheme remains stable without sub-iterations for light and even zero-mass bodies of general geometries in three dimensions.

The resultant algorithm has been verified and validated through several benchmark problems. It has been shown that the algorithm achieves a second-order accuracy and remains stable for some challenging problems. In particular, the benchmark problems involving particles have confirmed the algorithm is stable for very light bodies including a zero-mass body and the added-damping effects have to been handled properly to successfully simulate the problems. The linear system derived from the AMP interface condition has been

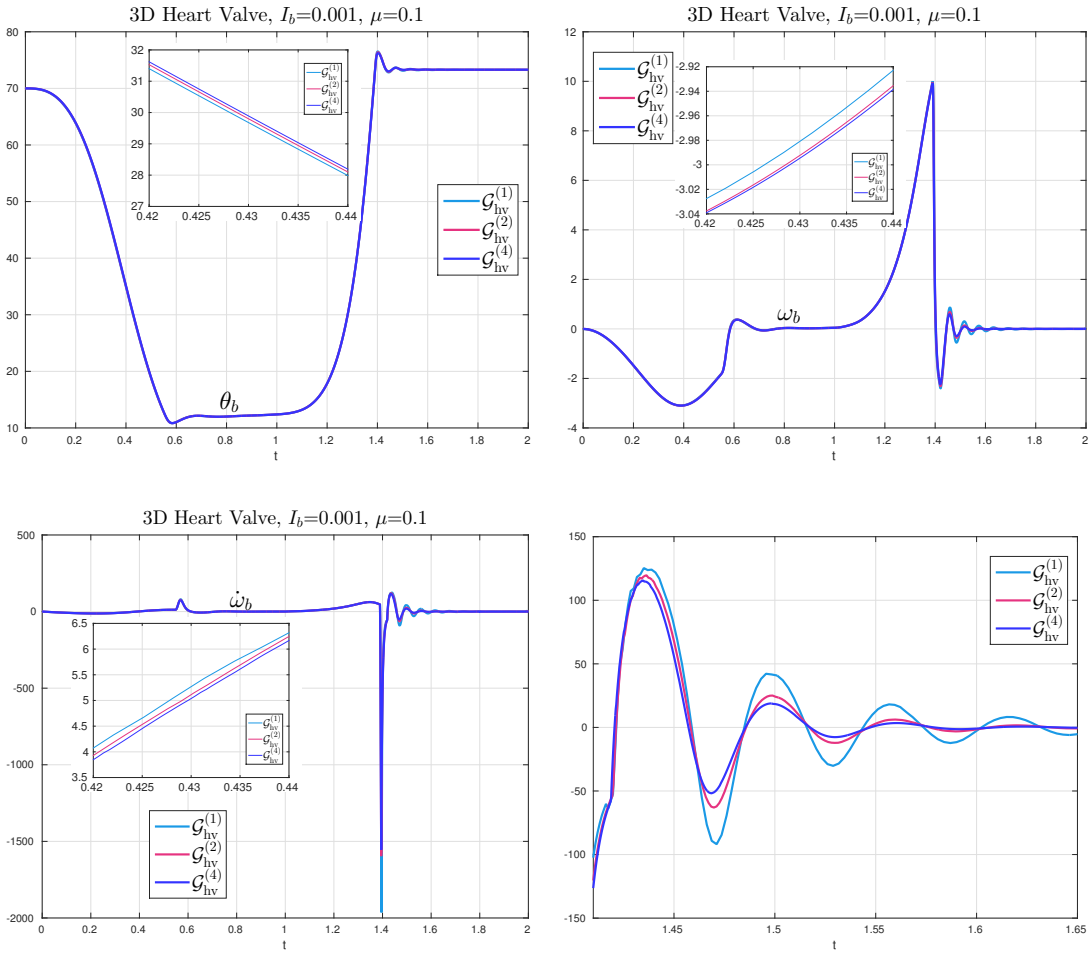

Figure 19: Mechanical heart valve in 3D. Time history of the rotation angle (top left), angular velocity (top right) and acceleration (bottom left) of the top leaflet. Several zoomed views are presented including the zoomed view of the accelerations at the later time (bottom right). Results are shown from calculations using the composite grid, $\mathcal{G}_{\rm hv}^{(j)}$, $j = 1, 2, 4$.

shown to have similar conditioning of a pressure Poisson system in a TP scheme. Benchmark problems involving mechanical heart valves show the applicability of the AMP-RB scheme to practical engineering problems and also demonstrate the advantageous of the AMP-RB scheme. All the benchmark problems have shown that the AMP-RB scheme is significantly more efficient than the TP scheme that requires sub-iterations to remain stable. The algorithm has been implemented in both serial and parallel, and the parallel performance test shows reasonable scaling.

A variety of future directions exist for this work. During the numerical investigation, it is found an algebraic multigrid solver (such as calling the Hypre package through PETSc) does not give good performance. This poor performance is mainly due to those entries corresponding to the interpolations from one grid to another in the linear system, see Figure 10 for instance. This motivates us to derive a geometrical multigrid solver for the current linear system by following the multigrid method in [58, 59]. The multigrid solver has been shown to be much faster and more memory efficient than Krylov solvers, but the multigrid solver needs to be extended to handle the AMP interface conditions. The parallel implementation of the full algorithm also needs more improvements. A particular attention will be focused on optimizing the parallel moving grid generator. The current simulation of the heart valve has some differences from the practical situation and needs improvements in various aspects including a realistic Reynolds number, a more accurate geometry of the leaflet and a practical boundary condition generalized from the experimental data. Those topics will be left for future work.

Appendix A. Collision model

Glowinski et al. [60] proposed a simple collision model based on a continuous repulsive force that depends on the distance between two rigid particles

$$\mathbf{F}(D) = \begin{cases} \mathbf{0} & \text{if} \quad D > R_1 + R_2 + \delta, \\ \frac{1}{\epsilon}\left(\frac{D - R_1 - R_2 - \delta}{\delta}\right)^2 \frac{\mathbf{x}_{b,1} - \mathbf{x}_{b,2}}{D} & \text{if} \quad D \le R_1 + R_2 + \delta. \end{cases}$$

Here D stands for the distance between the centers of two particles, of which the radii are R_1 and R_2 respectively. It is further suggested that the small distance is taken as $\delta \simeq \Delta s$ and the stiffness parameter is $\epsilon \simeq \Delta s^2$. This approach is widely used in FSI due to its simple formulation and straightforward implementation. In the implementation the force is only applied to the right hand side of the Newton-Euler equations as an external body force, while the FSI algorithms remain the same. In many simulations using this idea, δ is taken as $3\Delta s$ and ϵ is taken between 10^{-4} and 10^{-8}.

In the current work, this collision model has been extended to a repulsive torque applied to the leaflet in the mechanical heart valve in Section 5.5. In the literature, it appears that a post-processing approach is often used to restrict the rotation angle in the designed range, for instance, simply setting a hard limit on the range of the rotation angle. However, we find that such a post-processing approach leads to a significant mismatch between the leaflet speed and fluid velocity, and eventually the fluid solver becomes unstable. Note the mismatch in the AMP-RB scheme will not be diminished by sub-iterations while the sub-iterations may help to stabilize the TP-RB scheme in such a case.

Appendix A.1. A model problem for repulsive forces

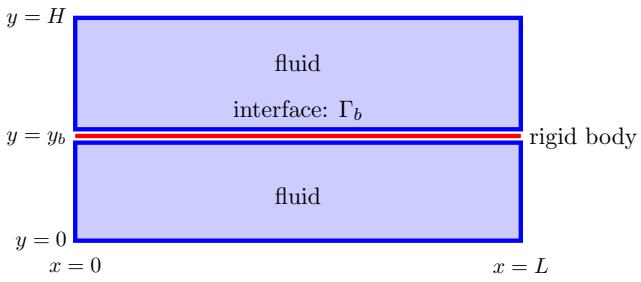

Figure A.20: The geometry for the model problem for repulsive forces.

In this section, a model problem is used to investigate the effects of the repulsive force and the damping term applied to the rigid body. Consider a rectangular rigid body of mass m_b immersed in an incompressible fluid. The geometry of the model problem is given in Figure A.20, in which a rigid body is located at y_b. The height of this rigid body has no effects in this case, and so the rigid body is assumed to be infinitely thin and denoted as a red line. The motion of the full system is driven by the pressure gradient between the top and bottom boundaries of fluid. We assume the pressure at $y = H$ is $p_H(t)$, the pressure at $y = 0$ is $p_0(t)$, and further assume $p_H(t) > p_0(t)$. A repulsive force $g_{\text{rf}}(y)$ is applied to the rigid body with

$$g_{\text{rf}}(y) = \begin{cases} 0 & \text{if} \quad y > y_0 + \delta, \\ \frac{1}{\epsilon}\left(\frac{y - y_0 - \delta}{\delta}\right)^2 & \text{if} \quad y_0 \le y \le y_0 + \delta, \\ \frac{1}{\epsilon} & \text{if} \quad y < y_0. \end{cases} \tag{A.1}$$

Initially, $y_b(0) > y_0 + \delta$. This repulsive force can be interpreted as a penalty that restricts the rigid body motion. Following similar arguments for the model problems in [1], this model problem can be assumed to

be only y-dependent. Therefore, the model with repulsive forces included (MP-RF) is given by

$$\text{MP-RF:}\begin{cases}\rho\dfrac{\partial v}{\partial t}+\dfrac{\partial p}{\partial y}=0, & y\in(0,y_b)\cup(y_b,H),\\ \dfrac{\partial v}{\partial y}=0, & y\in(0,y_b)\cup(y_b,H),\\ m_b\dfrac{dv_b}{dt}=L\left(p(y_b^-,t)-p(y_b^+,t)\right)+g_{\rm rf}(y_b)-B(y_b)\,v_b,\\ v(y_b^+,t)=v(y_b^-,t)=v_b,\quad p(H,t)=p_H(t),\quad p(0,t)=p_0(t).\end{cases}\tag{A.2}$$

Note that there is an extra damping term $B(y_b)\,v_b$ involved in the governing equation of the rigid body. Through numerical experiments, we find that it is important to involve a damping term to model the energy loss during the collision. The damping term is applied to the rigid body when the repulsive force is turned on. The damping coefficient $B(y)$ follows a similar fashion to $g_{\rm rf}(y)$ and is given by

$$B(y)=\begin{cases}0 & \text{if}\quad y>y_0+\delta,\\ B_0(\frac{y-y_0-\delta}{\delta})^2 & \text{if}\quad y_0\le y\le y_0+\delta,\\ B_0 & \text{if}\quad y<y_0,\end{cases}\tag{A.3}$$

with the coefficient $B_0>0$.

It is easy to show that the solutions of this model problem satisfy

$$v(y,t)=v_b(t),\tag{A.4}$$

$$(m_b+M_a)\frac{dv_b}{dt}=L\left(p_0(t)-p_H(t)\right)+g_{\rm rf}(y_b)-B(y_b)\,v_b,\tag{A.5}$$

with the added mass being $M_a=\rho LH$. Therefore, the effect of the whole fluid in this model problem is fully described by its added mass in the isolated equation of the rigid body motion (A.5). The isolated equation (A.5) can be normalized as

$$\frac{dv_b}{dt}=\tilde f(t)+\tilde g_{\rm rf}(y_b)-\tilde B(y_b)\,v_b.\tag{A.6}$$

Here $\tilde f(t)=L(p_t(t)-p_H(t))/(m_b+M_a)$, $\tilde g_{\rm rf}(y_b)$ and $\tilde B(y_b)$ follow the same formulations given in (A.1) and (A.3), respectively, except $\tilde\epsilon=\epsilon(m_b+M_a)$ and $\tilde B_0=B_0/(m_b+M_a)$.

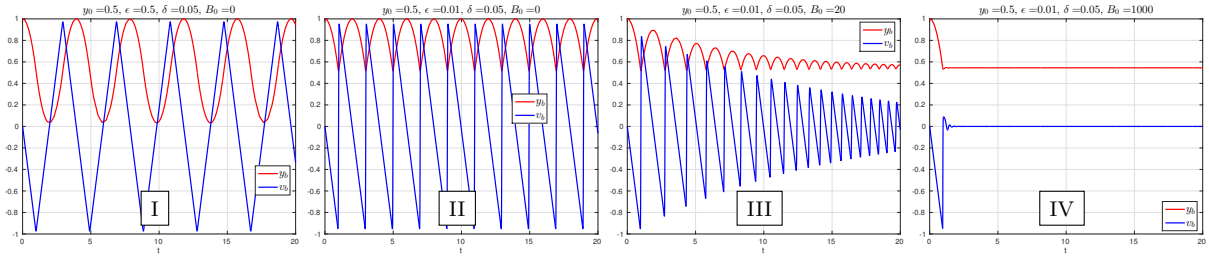

Figure A.21: MP-RF. Velocity and location of the rigid body. (I) ϵ is too large and there is no damping; (II) ϵ is small and there is no damping; (III) ϵ is small and the solution is under-damped; (IV) ϵ is small and the solution is over-damped.

For simplicity, we consider the case when $f(t)=-1$, the initial location of the rigid body is $y_b(0)=1$ with the speed $v_b(0)=0$, and the rigid body is assumed to collide at $y_0=0.5$. The results of some typical choices of the parameters $\tilde\epsilon$, δ and $\tilde B_0$ are presented in Figure A.21. In Case I, $\tilde\epsilon$ is too big so that the resulting repulsive force is too small to slow down the rigid body above y_0. In practice, this may lead to the interpenetration of multiple grids in the composite grid framework, which typically leads to the failure of simulation. In this case, the energy is not conserved due to the formulation of the repulsive force. In Case II, $\tilde\epsilon$ is small enough so that the repulsive force is able to slow down the rigid body before it hits the bound.

It is easy to show that the repulsive force conserves the total energy of the system in this case. Assume at the time τ, the height of the rigid body is $y_0 + \delta$ where the repulsive force starts to affect. Then the system satisfies,

$$\ddot{y}_b = -1 + \frac{1}{\tilde{\epsilon}}(\frac{y_b - y_0 - \delta}{\delta})^2, \tag{A.7}$$

with $\dot{y}_b(\tau) = v_\tau$ and $y_b(\tau) = y_0 + \delta$. Multiplying $\dot{y}_b$ at both side of (A.7) and integrating leads to

$$\frac{\dot{y}_b^2}{2} + y_b - \frac{1}{3\tilde{\epsilon}\delta^2}(y_b - y_0 - \delta)^3 = C, \tag{A.8}$$

which is true when the rigid body is in $[y_0, y_0 + \delta]$. The left hand side of (A.8) can be interpreted as the total energy of the system that consists of the kinetic energy, the potential energy and the energy related to the repulsive force. Therefore, the energy has been shown to be conserved without the damping term.

However, in some cases a significant amount of total energy can be lost through other complicated mechanisms during the collision. The damping term plays an important role in our model to model the energy loss. In Case (III), a damping term is turned on and the total energy of the system decays as the collision happens. The solution is under-damped and slowly converges to a constant. In Case (IV), a much larger damping term is used so that the motion of the rigid body is over-damped, in which case the solution quickly converges to a constant. This is useful to model the situation where significant amount of energy is lost during the collisions.

Appendix A.2. Applications to the heart valve simulations

In the mechanical heart valve simulations, the leaflets are designed to rotate only in a certain range of angles. Therefore, an extra mechanism is needed to force the leaflets stop before they cross the designed bounds. In the current simulations, this collision model has been used as the constraint on the range of the leaflet angle. Assume the range of the rotational angle of leaflets θ be $[\theta_{\min}, \theta_{\max}]$. The following external torque and damping term are used

$$g_{\rm rt}(\theta) = \begin{cases} \frac{1}{\epsilon_1} & \text{if} \quad \theta \le \theta_{\min}, \\ \frac{1}{\epsilon_1}(\frac{\theta - \theta_{\min} - \delta}{\delta})^2 & \text{if} \quad \theta_{\min} < \theta \le \theta_{\min} + \delta, \\ 0 & \text{if} \quad \theta_{\min} + \delta < \theta < \theta_{\max} - \delta, \\ -\frac{1}{\epsilon_2}(\frac{\theta - \theta_{\max} + \delta}{\delta})^2 & \text{if} \quad \theta_{\max} - \delta \le \theta \le \theta_{\max}, \\ -\frac{1}{\epsilon_2} & \text{if} \quad \theta > \theta_{\max}. \end{cases} \tag{A.9}$$

$$B(\theta) = \begin{cases} B_0 & \text{if} \quad \theta < \theta_{\min} \text{ or } \theta > \theta_{\max}. \\ B_0(\frac{\theta - \theta_{\min} - \delta}{\delta})^2 & \text{if} \quad \theta_{\min} < \theta \le \theta_{\min} + \delta, \\ 0 & \text{if} \quad \theta_{\min} + \delta < \theta < \theta_{\max} - \delta, \\ B_0(\frac{\theta - \theta_{\max} + \delta}{\delta})^2 & \text{if} \quad \theta_{\max} - \delta \le \theta \le \theta_{\max}, \end{cases} \tag{A.10}$$

This simple model can be interpreted as the results of the collision between the leaflets and the hinge, although the hinge is not explicitly described in the current simulation. Note the repulsive torque and damping term are a direct extension of the above collision model. This model shows much better performance in our implementation than simply setting a hard limit of the angles. The damping term is particularly important during the process of closing, where the significant amount of energy are lost through the collision between the leaflet and the hinge. See Section 5.5.

References

[1] J. W. Banks, W. D. Henshaw, D. W. Schwendeman, Q. Tang, A stable partitioned FSI algorithm for rigid bodies and incompressible flow. Part I: Model problem analysis, J. Comput. Phys. 343 (2017) 432–468.

[2] J. W. Banks, W. D. Henshaw, D. W. Schwendeman, Q. Tang, A stable partitioned FSI algorithm for rigid bodies and incompressible flow. Part II: General formulation, J. Comput. Phys. 343 (2017) 469–500.

[3] W. D. Henshaw, D. W. Schwendeman, Moving overlapping grids with adaptive mesh refinement for high-speed reactive and non-reactive flow, J. Comput. Phys. 216 (2) (2006) 744–779.

[4] N. Takashi, T. J. Hughes, An arbitrary Lagrangian-Eulerian finite element method for interaction of fluid and a rigid body, Comput. Method. Appl. Mech. Engrg. 95 (1) (1992) 115–138.

[5] H. H. Hu, N. A. Patankar, M. Y. Zhu, Direct numerical simulations of fluid-solid systems using the arbitrary langrangian-eulerian technique, J. Comput. Phys. 169 (2) (2001) 427–462.

[6] J. Vierendeels, K. Dumont, E. Dick, P. Verdonck, Analysis and stabilization of fluid-structure interaction algorithm for rigid-body motion, AIAA J. 43 (12) (2005) 2549–2557.

[7] M. Coquerelle, G.-H. Cottet, A vortex level set method for the two-way coupling of an incompressible fluid with colliding rigid bodies, J. Comput. Phys. 227 (21) (2008) 9121–9137.

[8] F. Gibou, C. Min, Efficient symmetric positive definite second-order accurate monolithic solver for fluid/solid interactions, J. Comput. Phys. 231 (8) (2012) 3246–3263.

[9] R. Glowinski, T.-W. Pan, T. I. Hesla, D. D. Joseph, A distributed Lagrange multiplier/fictitious domain method for particulate flows, Int. J. Multiphase Flow 25 (5) (1999) 755–794.

[10] S. D. Costarelli, L. Garelli, M. A. Cruchaga, M. A. Storti, R. Ausensi, S. R. Idelsohn, An embedded strategy for the analysis of fluid structure interaction problems, Comput. Method. Appl. Mech. Engrg. 300 (2016) 106–128.

[11] T. Kajishima, S. Takiguchi, Interaction between particle clusters and particle-induced turbulence, Int. J. Heat Fluid Flow 23 (5) (2002) 639–646.

[12] M. Uhlmann, An immersed boundary method with direct forcing for the simulation of particulate flows, J. Comput. Phys. 209 (2) (2005) 448–476.

[13] D. Kim, H. Choi, Immersed boundary method for flow around an arbitrarily moving body, J. Comput. Phys. 212 (2) (2006) 662–680.

[14] T.-R. Lee, Y.-S. Chang, J.-B. Choi, D. W. Kim, W. K. Liu, Y.-J. Kim, Immersed finite element method for rigid body motions in the incompressible Navier–Stokes flow, Comput. Method. Appl. Mech. Engrg. 197 (25) (2008) 2305–2316.

[15] I. Borazjani, L. Ge, F. Sotiropoulos, Curvilinear immersed boundary method for simulating fluid structure interaction with complex 3D rigid bodies, J. Comput. Phys. 227 (16) (2008) 7587–7620.

[16] W.-P. Breugem, A second-order accurate immersed boundary method for fully resolved simulations of particle-laden flows, J. Comput. Phys. 231 (13) (2012) 4469–4498.

[17] T. Kempe, J. Fröhlich, An improved immersed boundary method with direct forcing for the simulation of particle laden flows, J. Comput. Phys. 231 (9) (2012) 3663–3684.

[18] J. Yang, F. Stern, A simple and efficient direct forcing immersed boundary framework for fluid–structure interactions, J. Comput. Phys. 231 (15) (2012) 5029–5061.

[19] A. P. S. Bhalla, R. Bale, B. E. Griffith, N. A. Patankar, A unified mathematical framework and an adaptive numerical method for fluid–structure interaction with rigid, deforming, and elastic bodies, J. Comput. Phys. 250 (2013) 446–476.

[20] J. Yang, F. Stern, A non-iterative direct forcing immersed boundary method for strongly-coupled fluid–solid interactions, J. Comput. Phys. 295 (2015) 779–804.

[21] C. Wang, J. D. Eldredge, Strongly coupled dynamics of fluids and rigid-body systems with the immersed boundary projection method, J. Comput. Phys. 295 (2015) 87–113.

[22] Y. Kim, C. S. Peskin, A penalty immersed boundary method for a rigid body in fluid, Phys. Fluids 28 (3) (2016) 033603.

[23] U. Lācis, K. Taira, S. Bagheri, A stable fluid–structure-interaction solver for low-density rigid bodies using the immersed boundary projection method, J. Comput. Phys. 305 (2016) 300–318.

[24] E. Corona, L. Greengard, M. Rachh, S. Veerapaneni, An integral equation formulation for rigid bodies in stokes flow in three dimensions, J. Comput. Phys. 332 (2017) 504–519.

[25] R. Saye, Implicit mesh discontinuous Galerkin methods and interfacial gauge methods for high-order accurate interface dynamics, with applications to surface tension dynamics, rigid body fluidstructure interaction, and free surface flow: Part I, J. Comput. Phys. 344 (2017) 647–682.

[26] R. Saye, Implicit mesh discontinuous Galerkin methods and interfacial gauge methods for high-order accurate interface dynamics, with applications to surface tension dynamics, rigid body fluidstructure interaction, and free surface flow: Part II, J. Comput. Phys. 344 (2017) 683–723.

[27] A. R. Koblitz, S. Lovett, N. Nikiforakis, W. D. Henshaw, Direct numerical simulation of particulate flows with an overset grid method, J. Comput. Phys. 343 (2017) 414–431.

[28] C. Kadapa, W. G. Dettmer, D. Perić, A stabilised immersed boundary method on hierarchical b-spline grids for fluid-rigid body interaction with solid–solid contact, Comput. Method. Appl. Mech. Engrg. 318 (2017) 242–269.

[29] S. Schwarz, T. Kempe, J. Fröhlich, A temporal discretization scheme to compute the motion of light particles in viscous flows by an immersed boundary method, J. Comput. Phys. 281 (2015) 591–613.

[30] S. Tschisgale, T. Kempe, J. Fröhlich, A non-iterative immersed boundary method for spherical particles of arbitrary density ratio, J. Comput. Phys. 339 (2017) 432–452.

[31] R. Cheng, Y. G. Lai, K. B. Chandran, Three-dimensional fluid-structure interaction simulation of bileaflet mechanical heart valve flow dynamics, Ann. Biomed. Eng. 32 (11) (2004) 1471–1483.

[32] K. Dumont, J. Vierendeels, R. Kaminsky, G. Van Nooten, P. Verdonck, D. Bluestein, Comparison of the hemodynamic and thrombogenic performance of two bileaflet mechanical heart valves using a CFD/FSI model, J. Biomech. Eng. 129 (4) (2007) 558–565.

[33] C. H. Tai, K. M. Liew, Y. Zhao, Numerical simulation of 3D fluid–structure interaction flow using an immersed object method with overlapping grids, Comput. Struct. 85 (11) (2007) 749–762.

[34] M. Nobili, U. Morbiducci, R. Ponzini, C. Del Gaudio, A. Balducci, M. Grigioni, F. M. Montevecchi, A. Redaelli, Numerical simulation of the dynamics of a bileaflet prosthetic heart valve using a fluid–structure interaction approach, J. Biomech. 41 (11) (2008) 2539–2550.

[35] M. D. De Tullio, A. Cristallo, E. Balaras, R. Verzicco, Direct numerical simulation of the pulsatile flow through an aortic bileaflet mechanical heart valve, J. Fluid Mech. 622 (2009) 259–290.

[36] I. Borazjani, L. Ge, F. Sotiropoulos, High-resolution fluid–structure interaction simulations of flow through a bi-leaflet mechanical heart valve in an anatomic aorta, Ann. Biomed. Eng. 38 (2) (2010) 326–344.

[37] F. Sotiropoulos, I. Borazjani, A review of state-of-the-art numerical methods for simulating flow through mechanical heart valves, Med. Biol. Eng. Comput. 47 (3) (2009) 245–256.

[38] W. D. Henshaw, D. W. Schwendeman, Parallel computation of three-dimensional flows using overlapping grids with adaptive mesh refinement, J. Comput. Phys. 227 (16) (2008) 7469–7502.

[39] J. W. Banks, W. D. Henshaw, B. Sjögreen, A stable FSI algorithm for light rigid bodies in compressible flow, J. Comput. Phys. 245 (2013) 399–430.

[40] J. W. Banks, W. D. Henshaw, D. W. Schwendeman, Deforming composite grids for solving fluid structure problems, J. Comput. Phys. 231 (9) (2012) 3518–3547.

[41] J. W. Banks, W. D. Henshaw, A. Kapila, D. W. Schwendeman, An added-mass partitioned algorithm for fluid-structure interactions of compressible fluids and nonlinear solids, J. Comput. Phys. 305 (2016) 1037–1064.

[42] J. W. Banks, W. D. Henshaw, D. W. Schwendeman, An analysis of a new stable partitioned algorithm for FSI problems. Part I: Incompressible flow and elastic solids, J. Comput. Phys. 269 (2014) 108–137.

[43] J. W. Banks, W. D. Henshaw, D. W. Schwendeman, An analysis of a new stable partitioned algorithm for FSI problems. Part II: Incompressible flow and structural shells, J. Comput. Phys. 268 (2014) 399–416.

[44] L. Li, W. D. Henshaw, J. W. Banks, D. W. Schwendeman, G. A. Main, A stable partitioned FSI algorithm for incompressible flow and deforming beams, J. Comput. Phys. 312 (2016) 272–306.

[45] W. D. Henshaw, A fourth-order accurate method for the incompressible Navier-Stokes equations on overlapping grids, J. Comput. Phys. 113 (1) (1994) 13–25.

[46] N. A. Petersson, Stability of pressure boundary conditions for Stokes and Navier-Stokes equations, J. Comput. Phys. 172 (1) (2001) 40–70.

[47] W. D. Henshaw, Ogen: An overlapping grid generator for Overture, Research Report UCRL-MA-132237, Lawrence Livermore National Laboratory (1998).

[48] W. M. Chan, Enhancements to the hybrid mesh approach to surface loads integration on overset structured grids, AIAA paper 2009-3990.

[49] G. S. Chesshire, W. D. Henshaw, Conservation on composite overlapping grids, IBM Research Report RC 16531, IBM Research Division, Yorktown Heights, NY (1991).

[50] G. S. Chesshire, W. D. Henshaw, A scheme for conservative interpolation on overlapping grids, SIAM J. Sci. Comput. 15 (4) (1994) 819–845.

[51] W. D. Henshaw, Cgins user guide: An Overture solver for the incompressible Navier-Stokes equations on composite overlapping grids, Software Manual LLNL-SM-455851, Lawrence Livermore National Laboratory (2010).

[52] W. D. Henshaw, A high-order accurate parallel solver for Maxwell's equations on overlapping grids, SIAM J. Sci. Comput. 28 (5) (2006) 1730–1765.

[53] S. Balay, S. Abhyankar, M. F. Adams, J. Brown, P. Brune, K. Buschelman, L. Dalcin, V. Eijkhout, W. D. Gropp, D. Kaushik, M. G. Knepley, L. C. McInnes, K. Rupp, B. F. Smith, S. Zampini, H. Zhang, H. Zhang, PETSc users manual, Tech. Rep. ANL-95/11 - Revision 3.7, Argonne National Laboratory (2016).

[54] A. ten Cate, C. H. Nieuwstad, J. J. Derksen, H. E. A. V. den Akker, Particle imaging velocimetry experiments and lattice-boltzmann simulations on a single sphere settling under gravity, Physics of Fluids 14 (11) (2002) 4012–4025.

[55] N. Mordant, J.-F. Pinton, Velocity measurement of a settling sphere, Eur. Phys. J. B, Condens. Matter Complex Phys. 18 (2) (2000) 343–352.

[56] J. Yang, F. Stern, A sharp interface direct forcing immersed boundary approach for fully resolved simulations of particulate flows, J. Fluids Eng. 136 (4) (2014) 040904.

[57] W. D. Henshaw, An algorithm for projecting points onto a patched CAD model, Engineering with Computers 18 (2002) 265–273.

[58] W. D. Henshaw, G. S. Chesshire, Multigrid on composite meshes, SIAM J. Sci. Stat. Comput. 8 (6) (1987) 914–923.

[59] W. D. Henshaw, On multigrid for overlapping grids, SIAM J. Sci. Comput. 26 (5) (2005) 1547–1572.

[60] R. Glowinski, T.-W. Pan, T. I. Hesla, D. D. Joseph, J. Périaux, A distributed Lagrange multiplier/fictitious domain method for the simulation of flow around moving rigid bodies: application to particulate flow, Comput. Method. Appl. Mech. Engrg. 184 (2) (2000) 241–267.